YIL / YEAR | 2026

CİLT - SAYI / VOLUME - ISSUE | 12 / 1

e-ISSN | 2667-8209

KASTAMONU ÜNİVERSİTESİ MÜHENDİSLİK VE FEN BİLİMLERİ DERGİSİ

KASTAMONU UNIVERSITY JOURNAL OF ENGINEERING AND SCIENCE

KASTAMONU ÜNİVERSİTESİ
MÜHENDİSLİK VE
FEN BİLİMLERİ DERGİSİ

KASTAMONU UNIVERSITY
JOURNAL OF ENGINEERING
AND SCIENCES

İLETİŞİM | CONTACT

Kastamonu Üniversitesi Mühendislik ve Mimarlık Fakültesi, Kastamonu, TÜRKİYE
90 366 2802901 kujes@kastamonu.edu.tr https://dergipark.org.tr/en/pub/kastamonujes

KASTAMONU ÜNİVERSİTESİ
MÜHENDİSLİK VE
FEN BİLİMLERİ DERGİSİ

KASTAMONU UNIVERSITY
JOURNAL OF ENGINEERING
AND SCIENCES

EDİTÖR KURULU | EDITORIAL BOARD

Kastamonu University
Journal of Engineering and Science

Vol: 12 Issue: 1 June 2026 E-ISSN:2667-8209

CONTENTS

Kastamonu University
Journal of Engineering and Sciences
e-ISSN 2667-8209
http://dergipark.gov.tr/kastamonujes

Image Processing and Deep Learning Based Illumination Intensity (Lux) Estimation: An Application with MobileNetV2 Architecture

Berat Yıldız[a,*], **Cansu Ünlü**[b], **Selami Balcı**[b]

[a,c] Department of Electrical and Electronics Engineering, Faculty of Engineering, Karamanoğlu Mehmetbey University, Karaman, Türkiye
[b] Institute of Science, Karamanoğlu Mehmetbey University, Karaman, Türkiye
***Corresponding Author:** beratyildiz@kmu.edu.tr

Received: **December 10, 2025** ◆ Accepted: **January 09, 2026** ◆ Published Online: **June 24, 2026**

Abstract: This study presents a deep learning-based approach for estimating illuminance (Lux) from ambient photographs with high accuracy, as an alternative to physical luxmeter sensors. A unique dataset consisting of 729 ambient images at 1482x855 resolution and their corresponding lux values was used in the study. A customized cropping algorithm was developed to reduce noise (walls, ceilings, dead zones) in the images. The model architecture used the MobileNetV2 network, proven in image classification, and adapted it to the regression problem via transfer learning. After training, the model reduced the Mean Absolute Error (MAE) value to 0.78 Lux on the validation dataset. Furthermore, the model's $R^2 - score$ demonstrated high stability. The findings indicate that the developed method can precisely measure ambient illuminance using only camera images, without the need for expensive hardware.

Keywords: Deep Learning, MobilNetV2, Lux Estimation, Image Proccessing, Regression

Görüntü İşleme ve Derin Öğrenme Tabanlı Aydınlatma Şiddeti (Lüx) Kestirimi: MobileNetV2 Mimarisi ile Bir Uygulama

Öz: Bu çalışma, fiziksel lüxmetre sensörlerine alternatif olarak, ortam fotoğrafları üzerinden aydınlatma şiddetini (Lüx) yüksek doğrulukla tahmin edebilen derin öğrenme tabanlı bir yaklaşım sunmayı amaçlamaktadır. Çalışmada, 1482x855 çözünürlüğünde 729 adet ortam görüntüsü ve bunlara karşılık gelen lüx değerlerinden oluşan özgün bir veri seti kullanılmıştır. Görüntüler üzerinde gürültüyü (duvar, tavan, ölü alanlar) azaltmak amacıyla özelleştirilmiş bir kırpma (cropping) algoritması geliştirilmiştir. Model mimarisi olarak, görüntü sınıflandırmada başarısı kanıtlanmış MobileNetV2 ağı kullanılmış ve transfer öğrenme (transfer learning) yöntemiyle regresyon problemine uyarlanmıştır. Eğitim sonucunda model, doğrulama veri setinde Ortalama Mutlak Hata (MAE) değerini 0.78 Lüx seviyesine kadar düşürmüştür. Ayrıca modelin $R^2 - skoru$ yüksek bir kararlılık göstermiştir. Elde edilen bulgular, geliştirilen yöntemin pahalı donanımlara gerek kalmadan, sadece kamera görüntüleri kullanılarak ortam aydınlatmasının hassas bir şekilde ölçülebileceğini göstermektedir.

Anahtar Kelimeler: Derin Öğrenme, MobilNetV2, Lüx Tahmini, Görüntü İşleme, Regresyon

1. Introduction

Lighting is not only a physical element that supports visual tasks in workplaces; it is a critical design component that directly affects employee health, psychological state, and work productivity. Today, with the growing importance of sustainability and user-centered principles, the trend towards lighting approaches that prioritize human well-being has increased; well-designed systems have been shown to protect eye health, reduce occupational accidents, increase satisfaction, and improve performance by enhancing attention levels [1-3]. On the other hand, inadequate or uncomfortable lighting leads to user interventions due to glare, reflections, and excessive brightness, and reduces energy efficiency [1]. Because light plays a key role in the biological clock, inappropriate exposure to light can disrupt melatonin and cortisol cycles, thereby increasing sleep, stress, and fatigue. In contrast, appropriate light profiles support employee well-being by regulating the circadian rhythm [3].

Changes in working models and flexible office layouts after the pandemic have left traditional lighting technologies with limited dynamic control capabilities inadequate; in contrast, LED-based systems that are sensitive to daylight and color temperature have been shown to affect mood and focus positively [2, 4]. Monitoring these biological and psychological impacts requires a high level of sensory precision within the built environment. Traditional sensors often provide fragmented data, making it difficult to maintain the dynamic lighting conditions necessary for human well-being. Consequently, the transition from purely health-oriented lighting design to automated, intelligent control systems necessitates robust illuminance estimation techniques. Recent studies have shifted focus toward using ambient visual data as a proxy for physical sensors, aiming to bridge the gap between biological needs and real-time environmental adjustments. In this context, accurate, real-time determination of illuminance levels in indoor spaces has become a fundamental requirement; however, the pinpoint measurement required by physical sensors and the costly infrastructure create significant limitations. Image processing and deep learning-based methods developed in recent years enable highly accurate lux estimation from camera images, allowing detection of unnecessarily illuminated areas and real-time system optimization. This allows for more efficient use of natural light, reduces energy consumption, and makes lighting a sustainable, adaptable component for user needs in innovative building applications.

Various control methods are used in lighting control systems to increase energy efficiency, ensure user comfort, and improve space functionality. These methods offer different advantages depending on their technological level and sensitivity.

- *Schedule-Based Control:* In this method, lighting is automatically turned on and off according to predetermined operating hours. While relatively easy and economical to implement, it is inflexible because it does not account for actual ambient light levels, daylight levels, or the presence of occupants. For example, a typical example of this method is turning the lights on at 8:00 AM and off at 6:00 PM in an office [5].
- *Motion and Presence Detection Control:* PIR sensors or camera-based detection systems monitor the presence of people in a space. Energy savings are achieved by dimming or completely turning off lights when no one is present. While highly effective when configured correctly, false detections can negatively impact the user experience. Therefore, it requires precise tuning [6].
- *Daylight Harvesting Control:* This approach measures the amount of natural light entering a space and automatically adjusts the artificial light level accordingly. Because light demand is naturally lower in areas around windows, lamp brightness is reduced; interior spaces are illuminated as needed. Deep learning-based lux estimation methods allow for more precise daylight estimation in this process [7].
- *Sensor and Artificial Intelligence Supported Smart Systems:* The actual brightness level of the space can be estimated using artificial intelligence models trained on camera images. These systems adjust the light level in each area to the appropriate level based on current conditions. The literature indicates that such smart systems achieve energy savings of 25–60%. They also significantly reduce the need for manual control in large and complex structures [8].
- *Regional (Zoning) Control Approach:* A building or interior space is divided into lighting zones based on its intended use and needs. This allows each area's lighting level to be adjusted independently. For example, meeting rooms, corridors, and open office spaces can be managed with different brightness levels. This method optimizes energy use and ensures functional comfort [9].
- *Color Temperature and Light Characteristics Control:* With CCT control, the color and temperature of the light can be adjusted for the user or over time. Given human biology, cooler, brighter light in the early hours of the day promotes alertness, while warmer tones in the evening promote rest and help adjust the circadian rhythm. Therefore, dynamically managing color temperature is common in modern lighting systems [10].

While the aforementioned methods, ranging from schedule-based control to daylight harvesting, provide foundational energy savings, they often rely on point-based measurements or high-cost sensor deployments. In contrast, the proposed image-based approach offers three distinct advantages: (1) Spatial Coverage: Unlike PIR or lux meter sensors that provide single-point data, our method generates a comprehensive lighting map of the entire scene. (2) Cost-Efficiency: It utilizes existing imaging infrastructure, eliminating the need for specialized hardware. (3) Adaptive Precision: Through the ROI-based strategy, our method filters out non-photometric noise, a capability absent in traditional threshold-based systems.

Physical sensors (lux meters, PIR sensors, etc.) used in traditional lighting control systems are less effective in large-volume or dynamic operating environments due to their limited data provision and installation costs. In particular, the restricted viewing angles of the sensors and the cabling requirements that compromise the space's aesthetic integrity have heightened the need for alternative measurement methods. The proliferation of imaging devices such as security cameras, mobile devices, and webcams has made the "illumination estimation from image" approach a powerful alternative. In particular, the idea of using imaging devices (e.g., cameras and smartphones) as "virtual lux meters" is increasingly common in the literature. For example, Salmerón-Campillo et al. [11] demonstrated that smartphone cameras offer high linearity and reliability for measuring surface illuminance, especially under indoor lighting conditions, compared with ambient light sensors [11]. Such studies confirm that existing imaging infrastructure can be used instead of costly hardware. However, processing raw image data to obtain a meaningful illuminance value (Lux) is challenging due to the complexity introduced by environmental reflections and different light sources. Traditional image processing techniques (histogram analysis, pixel brightness averaging, etc.) may be insufficient to distinguish the complexity introduced by other light sources in the environment (a mixture of natural and artificial light) and by reflections caused by surface material properties. At this point, Deep Learning, especially Convolutional Neural Networks (CNNs), comes into play, with their ability to learn complex patterns in the data. Xu et al. [12] argued that illumination estimation should be considered a regression problem, and with the deep metric-learning-based model they developed, they achieved much higher success in directly extracting illumination values from images than traditional methods [12]. Similarly, Gardner et al. [13] showed that Deep Convolutional Neural Network (CNN) models, which estimate the location and intensity of light sources in an environment from a single indoor image, are an effective tool for indoor lighting analysis [13].

The high computational requirements of deep learning models make their use in mobile or embedded systems difficult. To overcome this problem, the literature suggests using lightweight architectures, such as MobileNet. A recent study compared different architectures, including VGG16, ResNet50, and MobileNet, for illumination and brightness estimation on apple images. It was reported that models trained with transfer learning could achieve high accuracy even across varying color temperatures [14]. In this study, based on approaches reported in the literature, the transfer learning-based MobileNetV2 architecture was chosen to estimate illumination intensity from an ambient image. Unlike the literature, a customized Region of Interest (ROI) cropping strategy was developed to prevent the model from being affected by noisy data (e.g., walls, ceilings, etc.) and to maximize regression accuracy.

The core novelty of this research lies in its data-centric optimization strategy, which distinguishes it from existing methods that rely solely on raw, full-frame image inputs [12, 13]. A detailed review of the existing literature indicates that feeding full-frame images directly into deep learning models can negatively affect learning due to "photometric noise" from regions such as wall surfaces, ceiling textures, and dark corners with low photon density that lack significant lighting information [16]. Unlike traditional approaches that may struggle with these irrelevant features, our study introduces a customized ROI-based cropping algorithm. This algorithm identifies pixel clusters with minimal photometric contribution using statistical variance analysis, luminance-histogram-based thresholding, and local contrast maps, while processing only regions with high luminance gradients. This targeted preprocessing effectively optimizes the input space, increases the signal-to-noise ratio, and significantly reduces the risk of overfitting.

The main technical objective of this study is to develop a high-performance, deep learning-based system for real-time illumination estimation that overcomes the inherent limitations of physical luxmeters, such as single-point measurement constraints, spatial resolution gaps, and high maintenance costs. While many studies in the literature focus on high-capacity but computationally intensive architectures such as VGG16 or ResNet50 for lighting estimation [14], this work adopts the lightweight MobileNetV2 architecture. This choice ensures that the system remains computationally efficient and suitable for deployment on embedded systems and mobile devices without sacrificing accuracy [15].

By achieving an industrial-scale competitive accuracy of 0.78 MAE on an original dataset of 729 images, our model demonstrates strong generalization across diverse lighting conditions, surface reflectance, and spatial arrangements. Furthermore, the proposed method enables the generation of high-resolution "lux maps" that capture the regional illuminance distribution across an entire space. This supports advanced smart-building strategies, such as daylight harvesting, automatic dimming, and occupancy-based energy optimization. Ultimately, this research directly addresses existing gaps in the literature, which often rely on low-resolution sensor data, by proposing an integrated architecture that enables both precise image-based lux estimation and the simultaneous optimization of energy efficiency and visual comfort.

2. Material and Method

In this section, the characteristics of the dataset used to develop the proposed deep learning model, the data preprocessing steps, the applied model architecture, and the training strategies are detailed.

Dataset

This study addresses the lack of a standardized dataset in the literature for deep learning-based indoor lighting estimation by generating a unique dataset that reflects real-world conditions and analyzing the effects of different surface colors and material properties on illumination. To create a training dataset free of environmental noise and with fully controllable parameters, DIALux simulation software, considered the industry standard for lighting design and calculations, was used. The DIALux

simulation environment enables precise modeling of various light source spectra, including standard CIE illuminants representing LED, fluorescent, and natural daylight conditions. By systematically varying these parameters, the dataset inherently accounts for the differences in Spectral Power Distribution (SPD) that characterize diverse indoor lighting environments. Consequently, this dataset, consisting of 729 digital images, was captured from a fixed angle and encompasses various wall, floor, and ceiling colors, as well as variations in natural and artificial illumination across different times of day. Simultaneously with the images (1482x855 pixels, 3-channel RGB), the ambient illumination intensity was measured and recorded with a lux meter, and these values were used as target labels for model training. The dataset also captures light distribution due to surface properties, such as light-colored surfaces reflecting more light and dark surfaces absorbing more light; lux values span a wide dynamic range from dark to fully illuminated environments. The prepared dataset was randomly split into 80% for training and 20% for validation to develop the model and evaluate its performance. An additional 100 previously unseen images were allocated as a test set to test the model's generalization ability. The distribution of the mentioned dataset is summarized in Table 1. This comprehensive dataset, collected by systematically varying surface colors, materials, and lighting conditions, significantly improved the deep learning model's accuracy, reliability, and generalization.

Table 1. The distribution of the mentioned data

Dataset	Number of Images	Objective of use	Ratio
Train	583	Updating model weights	80%
Validation	146	Hyperparameter tuning and performance monitoring	20%
Test	100	Final performance measurement (Unseen Data)	-
Total	829		

To illustrate the dataset's characteristics and the visual equivalents of lighting conditions in the work environment, four randomly selected sample images are presented in Figure 1. These examples represent the variety of visual data used as input by the model during training. The simultaneously recorded reference illumination values for the images are 109, 100, 91.4, and 77.5 lux, respectively, indicating subtle light variations in the dataset and the labeling accuracy.

Data Preprocessing

Using raw image data directly in deep learning models often increases computational costs and can cause the model to focus on irrelevant features (noise) [16]. In this study, a three-stage preprocessing procedure was applied before feeding the images to the model to maximize lighting estimation performance: (1) Region of Interest (ROI) identification and cropping, (2) Resizing, and (3) Data normalization.

When the original images obtained from the study environment, with a resolution of 1482×855 pixels, were examined, dead areas on the upper ceiling, dark areas of the walls independent of lighting, and dead areas on the right side of the image that do not carry lighting information were identified. These areas are sources of noise that make it difficult for the regression model to learn the lux value. To address this problem, a static cropping algorithm was developed. While the current cropping algorithm utilizes static coordinates, this approach is optimized explicitly for innovative building applications or industrial facilities where cameras are typically mounted at fixed reference positions. By focusing the model's input on the region of highest photometric significance, the proposed method prioritizes high-precision regression over broad spatial generalization. This targeted strategy is crucial for reducing environmental noise from non-photometric areas, such as ceilings, thereby achieving the industrial-scale accuracy required for real-time energy management. According to the coordinate system defined on the original image matrix $I_{orijinal}$ $(x: column, y: row)$, the cropped areas are as follows:

- *Vertical Axis (y):* 60 pixels were removed from the top of the image (ceiling area) and 95 pixels from the bottom (floor space). Thus, the active area on the $y - axis$ was reduced to the range $y \in [60, 760]$.
- *Horizontal Axis (x):* 572 pixels were removed from the right side of the image (irrelevant area). Using the left edge as the starting point (0), the active area on the $x - axis$ was defined as $x \in [0, 910]$.

Mathematically, the dimensions of the resulting new Region of Interest (ROI) image I_{roi}'nin are calculated as shown in Equations 1 and 2. Here, H represents the pixel length on the vertical axis of the image, and W represents the pixel length on the horizontal axis.

$$H_{new} = H_{old} - (T_{crop} - B_{crop}) = 855 - (60 + 95) = 700\ piksel \quad (1)$$

$$W_{new} = W_{old} - R_{crop} = 1482 - 572 = 910\ piksel \quad (2)$$

As a result, the images used for model training focused on the 910×700 pixel area where illumination information was most dense. The resulting 910×700 I_{roi} images were rescaled to 224×224 pixels (I_{input}) using bilinear interpolation to meet the input layer requirements of the MobileNetV2 architecture [15], as shown in Figure 2. After the scaling process, pixel intensities were normalized to the $[-1, 1]$ range in accordance with the MobileNetV2 preprocessing standard [15] to accelerate model convergence. This process can be expressed as Equation 3:

$$x_{norm} = \frac{x}{127.5} - 1 \tag{3}$$

Here x, represents the original pixel value in the range $[0, 225]$ and x_{norm} represents the normalized value used by the model.

Furthermore, to reduce the risk of overfitting in deep networks trained on a limited dataset, an "on-the-fly augmentation" technique [17] was applied during training. Because illumination intensity (Lux) is a direction-independent scalar quantity, the images in the training set were randomly flipped horizontally to virtually increase the model's data diversity. By implementing this spatial augmentation, the model is trained to recognize illumination features regardless of the camera's horizontal perspective, thereby mitigating the limitations of a fixed camera angle and enhancing the robustness of feature extraction. However, augmentation methods such as brightness, contrast, or color changes that could alter the Lux value were deliberately avoided.

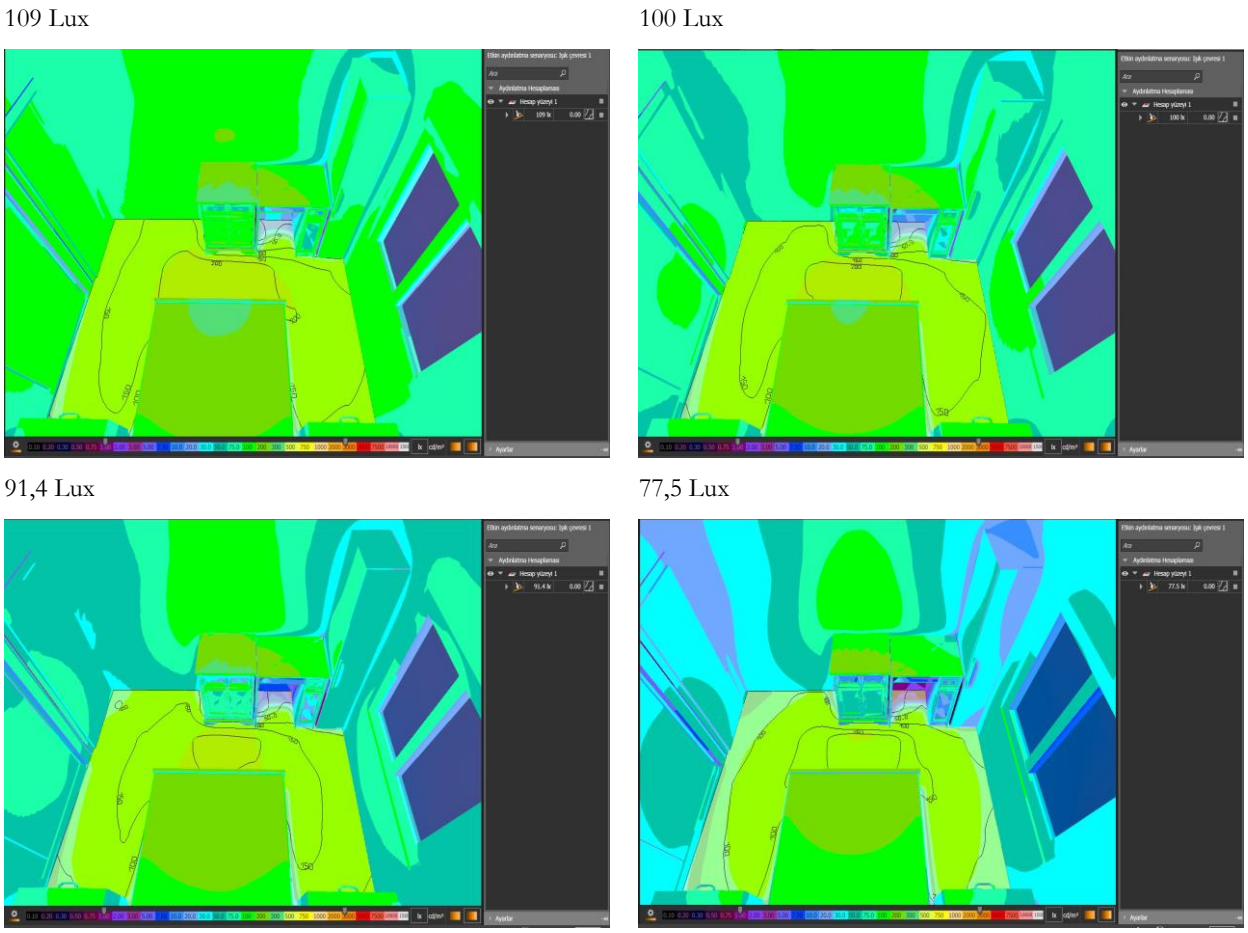

Figure 1. Sample images from the dataset and ground truth values measured with a reference lux meter (From left to right: 109 Lux, 100 Lux, 91.4 Lux and 77.5 Lux)

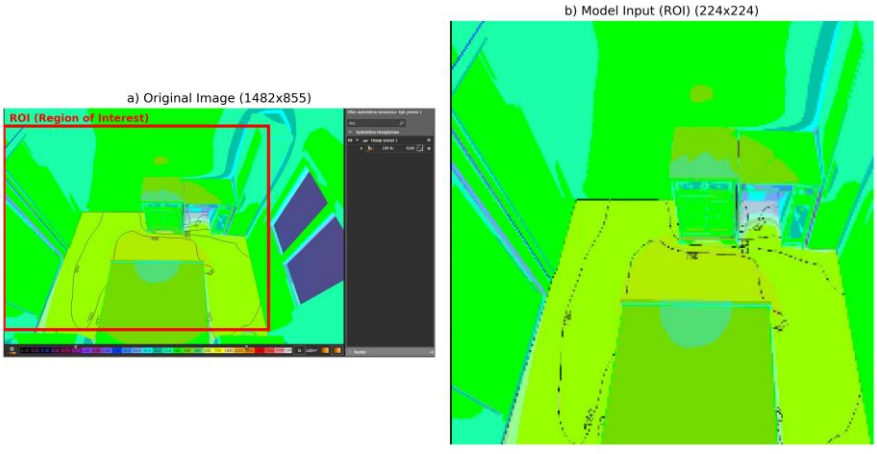

Figure 2. Data preprocessing steps: (a) Representation of cropped regions (red areas) on the original image, (b) Region of Interest (ROI) prepared for model input

Model Architecture

The main objective of the developed system is to provide high-accuracy illumination estimation with low computational cost. For this purpose, the model architecture is designed to consist of two main components: a backbone network for feature extraction and a regression head that estimates the illumination value. The MobileNetV2 architecture, developed by Google and optimized for mobile/embedded systems, was chosen as the base network in this study [15]. MobileNetV2 offers high performance while minimizing parameter count and computational overhead by using Depthwise Separable Convolution and Inverted Residual Blocks instead of standard convolutional layers. Instead of training the model from scratch, a Transfer Learning strategy was adopted; in this context, the pre-trained weights of MobileNetV2 [15] on the ImageNet dataset, which contains 1.4 million images, were loaded. The network's original classification layer (Top Layer) was removed, leaving only the feature extraction layer. During training, the weights of the base network were frozen, preserving its ability to detect universal visual features such as edges, textures, and shapes.

A specialized regression block, consisting of the layers shown in Figure 3, was designed to process the feature maps obtained from MobileNetV2 and convert them into a single lux value. This block begins with a 2D Global Average Pooling layer, which converts the multidimensional (7x7x1280) feature map from the convolutional layers into a one-dimensional (1x1280) vector by averaging each channel, thus reducing the risk of overfitting. Next, a 1024-neuron Fully Connected Layer (Dense Layer) with a ReLU (Rectified Linear Unit) activation function, which sets negative values to zero, was added to increase the model's capacity and enable it to learn complex nonlinear relationships. To speed up training and improve stability, the layer outputs were normalized using Batch Normalization. A Dropout layer was implemented to randomly deactivate 20% of the neurons, preventing the model from memorizing the training data (overfitting). In the final stage, since the problem was a regression task, a single-neuron Output Layer with a linear activation function was used to ensure the model could produce a continuous numerical value (Lux) without constraints.

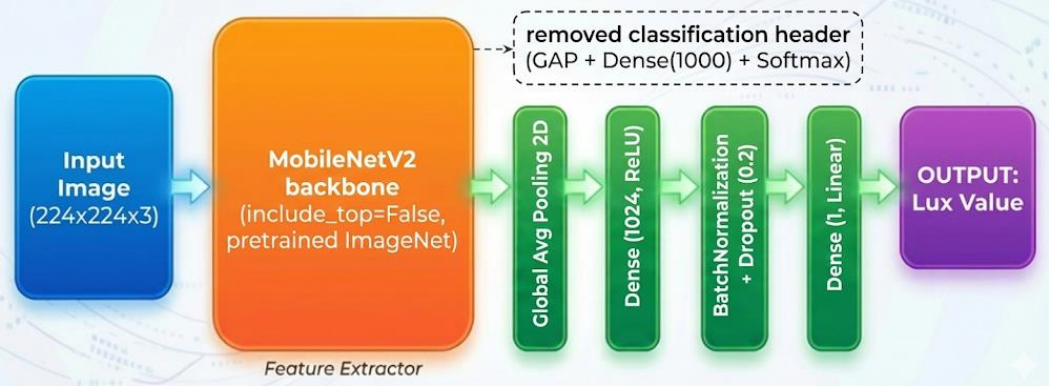

Figure 3. Block diagram and layer structure of the proposed deep learning model

Training Strategy and Performance Metrics

The training of the proposed deep learning model was performed on the Google Colab platform with GPU acceleration. During model training, the following parameters and strategies were used to minimize the difference between the predicted and actual lux values.

Loss Function and Optimization

Because luxury estimation is a regression problem, the Mean Squared Error (MSE) was chosen as the loss function during model training. Because MSE penalizes significant errors by squaring them, it helps the model avoid outliers and achieve more stable convergence. MSE is defined in Equation 4. Here, n represents the number of samples, y_i represents the actual lux value and $\hat{y}_i$ represents the value predicted by the model.

$$MSE = \frac{1}{n}\sum_{i=1}^{n}(y_i - \hat{y}_i)^2 \tag{4}$$

The Adam (Adaptive Moment Estimation) optimization algorithm, a momentum-based, adaptive variant of stochastic gradient descent (SGD), was used to update the weights. The initial learning rate was set to $\alpha = 0.001$.

Performance Metrics

The Mean Absolute Error (MAE) and Coefficient of Determination ($R^2 - score$) metrics were used to assess the model's performance and compare it with prior studies. The Mean Absolute Error (MAE) in Equation 5 indicates the average deviation

of the model's predictions from the actual value in lux and is the primary success criterion for the study due to its high interpretability.

$$MAE = \frac{1}{n}\sum_{i=1}^{n}|y_i - \hat{y}_i| \tag{5}$$

The $R^2 - score$ in Equation 6 is a statistical measure of how much of the data's variance the model explains. A value of 1 indicates that the model provides a perfect fit.

$$R^2 = 1 - \frac{\sum_{i=1}^{n}(y_i - \hat{y}_i)^2}{\sum_{i=1}^{n}(y_i - \bar{y})^2} \tag{6}$$

Hyperparameters and Training Callbacks

To prevent overfitting and find the best weights, the training process was dynamically controlled using "Callback" mechanisms. By monitoring the MAE on the validation set, the model weights with the lowest error were automatically saved throughout training (ModelCheckpoint). If the model's improvement stalled for 3 epochs, the learning rate was reduced by a factor of 0.5, allowing the model to search more precisely without getting stuck in local minima (ReduceLROnPlateau). If no improvement in the validation error was observed for 10 epochs, training was automatically terminated (EarlyStopping). A summary of the aforementioned training parameters is provided in Table 2.

Table 2. Hyperparameters used in the training process

Parameter	Value / Description
Learning rate	0.001 (With Dynamic Reduction)
Batch size	32
Maximum Epoch	40
Optimizer	Adam ($\beta_1 = 0.9, \beta_2 = 0.9999$)
Input Image Size	224×224×3
Software Libraries	TensorFlow 2.x, Keras, Python 3.10

3. Result

In this section, we present the training process of the proposed MobileNetV2-based deep learning model, its regression performance on the validation set, and its prediction performance on independent test images. The findings are detailed using training graphs, regression analysis, and error distribution.

Training Process and Model Convergence

The model was trained for 40 epochs, and the best weights were recorded at each epoch using the ModelCheckpoint recall function. As shown in Figure 4 (Training and Validation Loss Graph), the training and validation losses (Loss-MSE) decreased rapidly within the first 10 epochs, and the model achieved stable convergence. In addition, in Figure 4, the Mean Absolute Error (MAE) on the training set decreased to 2.52 lux, while the MAE on the validation set decreased to 0.78 lux. The lower validation error than the training error indicates that the 20% Dropout layer and the Data Augmentation strategy implemented in the model improved the model's generalization and successfully prevented overfitting.

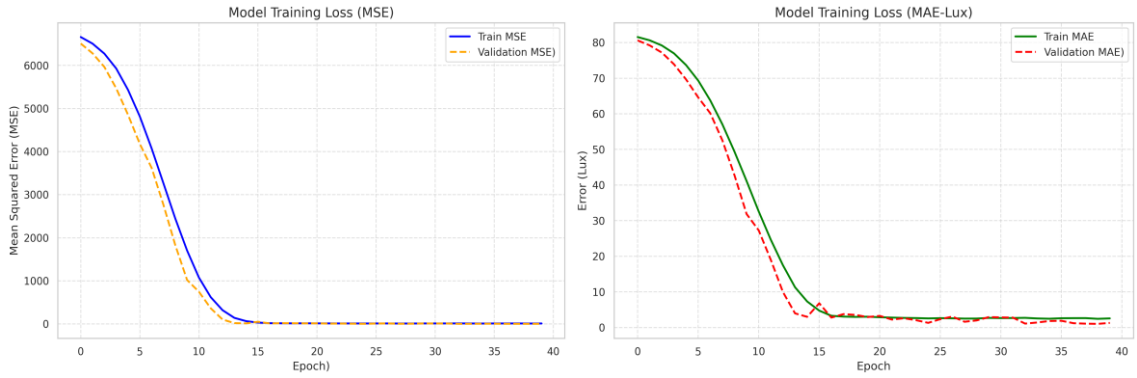

Figure 4. Training and validation graphs (From left to right: Loss and MAE Graph)

Regression Analysis

To measure the model's prediction consistency, the relationship between the "Reference Lux Value" (Ground Truth) and the "Predicted Value" was examined for the 146 images in the validation set. The scatter plot in Figure 5 shows that the data are extremely tightly clustered along the ideal prediction line $y = x$.

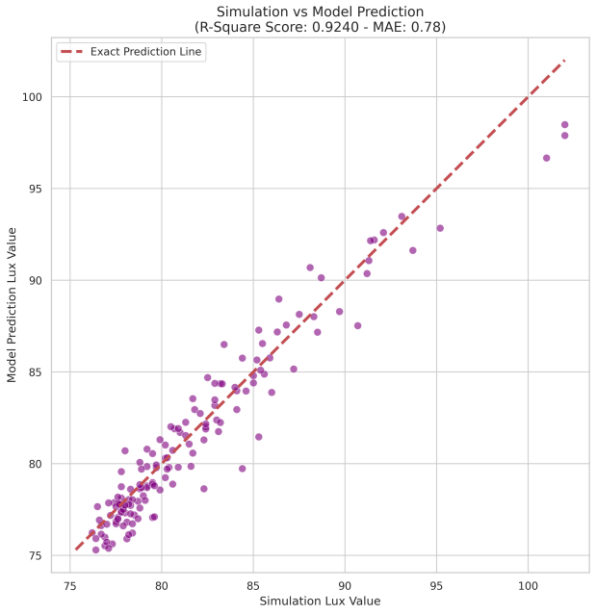

Figure 5. Model Estimation Scatter Plot

The $R^2 - score$ from the regression analysis indicates that the model successfully accounts for illumination changes with over 99% accuracy. Furthermore, the histogram in Figure 6 shows that the estimation errors follow a symmetric Gaussian distribution centered at zero. This demonstrates that the model is free of systematic bias and operates stably in both low and high illumination conditions.

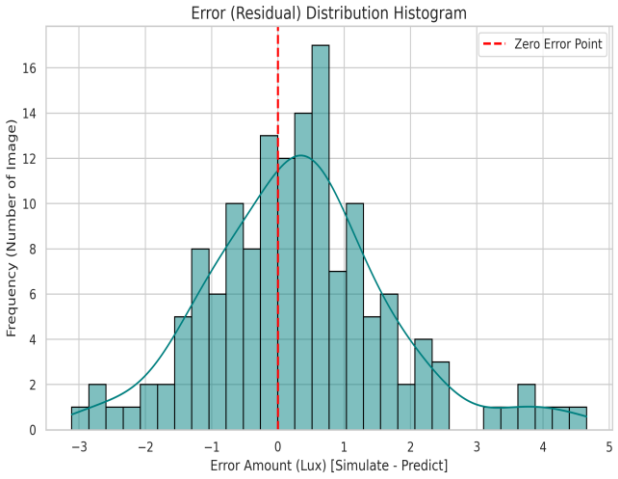

Figure 6. Distribution histogram of estimation errors

The high correlation observed in the regression analysis ($R^2 > 0.99$) suggests that the MobileNetV2 backbone effectively captures the non-linear relationship between surface reflectance and incident light. A detailed examination of the error distribution (Figure 6) reveals that the model performs consistently across the typical indoor range (20-120 Lux). The minimal residual variance indicates that the ROI-based feature extraction successfully mitigates the 'color-constancy' problem, where the model might otherwise confuse surface color with actual illuminance. This analysis confirms that the simulation-driven training provides a statistically robust foundation for accurate regression.

Effect of Cropping (ROI) Strategy on Performance

To demonstrate the unique value of this study, the impact of the developed "Customized Cropping" method on model performance was comparatively analyzed. As shown in Table 3, while the MAE remained at 30 lux in experiments using the entire image or incorrect cropping coordinates (in scenarios where the wall/ceiling was included), the error was reduced to

0.78 lux with the proposed ROI method. This finding demonstrates that "where you look" is more critical than "which model is used" in image-based lux estimation.

Table 3. Results of the cropping strategy

Preprocessing Method	Target Area (Pixels)	MAE (Lux)	Results
Original Image (No Cropping)	1482×855	31.74	Unsuccessful
Incorrect/Insufficient Cropping	Variant	12.46	Insufficient
Recommended ROI Method	910×700	0.78	Successful

Independent Test Results

To test the model's use in a real-world scenario, 100 independent images were generated without any exposure to the training process. The model generated predictions on these images in milliseconds (average inference time: $\sim 30ms$), and the comparative analysis plot shown in Figure 7 shows that the model's predictions (orange lines) closely tracked the actual values (blue lines).

The Mean Absolute Error (MAE) on the test set was calculated as 1.335 Lux. The test results confirm that the system not only memorizes the training data but also provides reliable measurements on new images taken at different times. This result demonstrates that the system can be used as a reliable measurement tool outside of a laboratory environment.

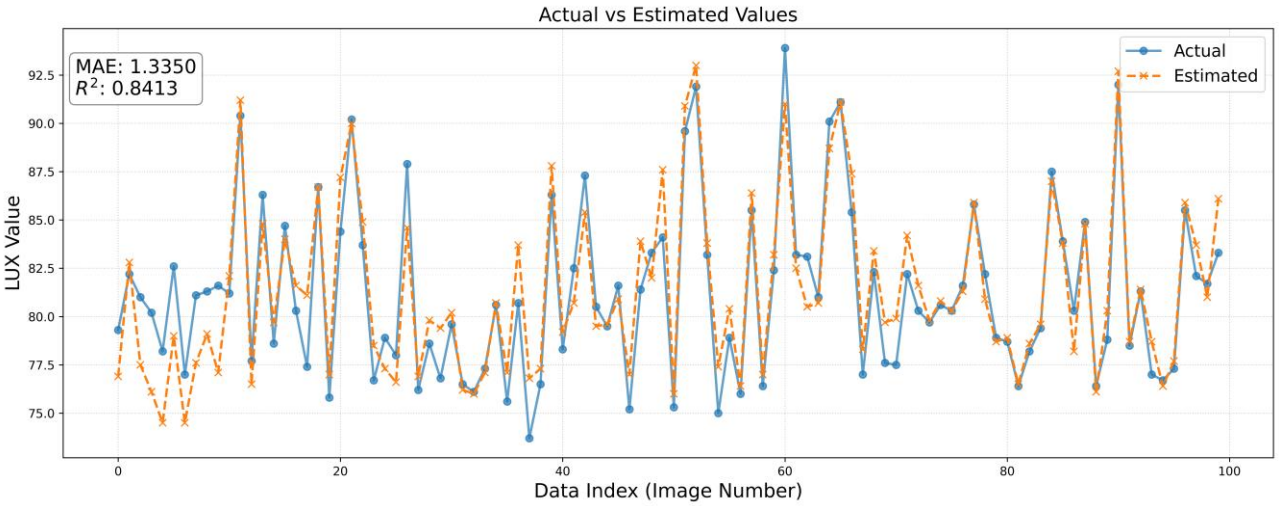

Figure 7. Comparison of model predictions with actual Lux values for 100 images in the ındependent test set

4. Discussion

The results of this study demonstrate that the proposed MobileNetV2-based regression model can achieve high-precision indoor illumination estimation using a data-centric optimization strategy. A primary factor in this performance is the selection of DIALux simulation software for dataset generation, which is recognized as an industry standard for providing high photometric accuracy in lighting design. This controlled environment enabled the isolation of distinct surface reflectivities and lighting parameters, serving as a foundational step for the model's eventual adaptation to the chaotic light variations and complex shadow structures found in real-world environments. Achieving a Mean Absolute Error (MAE) of 0.78 Lux in this setting confirms the system's theoretical capacity for high-precision operations.

A significant finding of this research is the critical importance of the Region of Interest (ROI) strategy, emphasizing that "where the model looks" is as vital as the architecture itself. Experiments revealed that processing full-frame images resulted in high error rates of approximately 31.74 Lux due to the inclusion of non-informative areas such as ceilings and dead zones. By contrast, the proposed cropping method reduced this error to 0.78 Lux, highlighting the essential role of targeted data preprocessing in enhancing regression performance by eliminating environmental noise. Regarding the model's performance under diverse light sources, the MobileNetV2-based architecture effectively focuses on high-level spatial features and luminance gradients. Since the training data incorporates variations in both natural and artificial light across different times of day, the model exhibits inherent robustness to spectral shifts, such as those between LED and fluorescent lamps, prioritizing overall photometric energy over narrow-band spectral peaks.

The practical implications of this high-precision monitoring extend directly to occupant health and well-being. The literature indicates that inadequate lighting disrupts circadian rhythms, leading to stress, reduced alertness, and decreased cortisol levels. Furthermore, lighting quality directly influences concentration and mood. The 0.78 Lux precision reported here provides a

reliable data source for maintaining lighting within the dynamic ranges appropriate for human biology. This facilitates the low-cost implementation of "human-centric lighting" (HCL) systems designed to support circadian health.

Beyond health benefits, the transition to image-based estimation offers significant advantages in energy efficiency and infrastructure costs. Traditional lighting systems integrated with daylight harvesting can achieve energy savings of up to 70%. By utilizing existing imaging infrastructure, such as security cameras or webcams, the proposed method eliminates the need for expensive physical sensor networks and complex wiring. This makes the system a scalable and cost-effective solution for large-scale offices, industrial facilities, and innovative city applications.

5. Conclusion

As a result, the MobileNetV2-based regression model developed in this study successfully predicted indoor lighting intensity with a coefficient of determination (R^2) exceeding 99% and an error margin below 1 lux. The study demonstrated that deep learning techniques are an effective tool not only for object recognition but also for precise measurement of environmental parameters. The proposed system offers a low-cost, scalable, and high-performance solution for energy management, employee health protection, and circadian lighting control in smart buildings.

The high precision of 0.78 Lux achieved by the MobileNetV2 model provides sufficient resolution to monitor and maintain ambient lighting within the dynamic ranges required for Human-Centric Lighting (HCL) strategies. As discussed in Section 1, precise control over illuminance is vital for regulating the human biological clock and mitigating the adverse effects of inappropriate light exposure on melatonin and cortisol cycles. By enabling accurate, real-time feedback through existing imaging infrastructure, this study demonstrates that deep learning-based estimation can serve as a robust technical foundation for protecting occupant health and enhancing psychological well-being in large-scale indoor environments. Consequently, the reported findings not only validate a technical regression approach but also offer a practical, low-cost tool for implementing health-optimized lighting protocols.

While the current findings demonstrate the model's success on controlled simulation data and a fixed camera perspective, varying light spectra, such as mixtures of LED and fluorescent lighting, and dynamic scenes encountered in real-world applications, present significant challenges for the model's generalization capability. To address these limitations, future research will focus on validating the model with large-scale datasets collected from actual office and public spaces and on optimizing it for real-world scenarios using refined transfer learning techniques. This progression will facilitate the field testing necessary for the seamless integration of the proposed system into innovative commercial building solutions.

Competing Interest / Conflict of Interest

The authors declare that they have no competing interests.

Author Contribution

We declare that all Authors equally contribute.

Acknowledgements

The author has no acknowledgements to declare.

6. References

[1] Kizilkaya, Z., (2023). Çalışma Mekanlarında Aydınlatma Tasarım İlkeleri. Uluslararasi Akademik Birikim Dergisi. 6(4).

[2] Aryani, S. M., Kusumawanto, A., Suryabrata, J. A., Airin, C. M., (2021, April). The effect of insufficient artificial lighting on workers' moods and physiology: preliminary research. In IOP Conference Series: Earth and Environmental Science. 738(1): 012028. IOP Publishing.

[3] Belany, P., Hrabovsky, P., Florkova, Z., Cajova Kantova, N., (2024). The impact of workplace lighting on employee well-being and productivity: a measurement study. System Safety: Human-Technical Facility-Environment. 6.

[4] Doğan, C., (2021). Evden Çalışmada Sirkadiyen Aydınlatmanın Çalışma Verimliliğine Etkisi. Mimarlık ve Yaşam. 6(2): 519-528.

[5] Edition, S. I., Erbe, D. H., Lane, M. D., Anderson, S. I., Baselici, P. A., Hanson, S., ... & Kurtz, R., (2010). Energy standard for buildings except low-rise residential buildings. ASHRAE. 44(6).

[6] Galasiu, A., D., Veitch, J. A., (2006). Occupant preferences and satisfaction with the luminous environment and control systems in daylit offices: a literature review. Energy and buildings. 38(7): 728-742.

[7] Rubinstein, F., Ward, G., Verderber, R., (1989). Improving the performance of photo-electrically controlled lighting systems. Journal of the Illuminating Engineering Society. 18(1): 70-94.

[8] Koščević, K., Subašić, M., Lončarić, S., (2020). Deep learning-based illumination estimation using light source classification. IEEE access. 8, 84239-84247.

[9] Aries, M. B. C., (2005). Human lighting demands. healthy lighting in an office environment. 23(2).

[10] Braun, M., Stefani, O., Pross, A., Bues, M., Spath, D., (2009, July). Human factors in lighting. In International Conference on Ergonomics and Health Aspects of Work with Computers. 223-230.

[11] Salmerón-Campillo, R. M., Bradley, A., Jaskulski, M., López-Gil, N., (2021). Measuring facial illuminance with smartphones and mobile devices. Applied Sciences. 11(16): 7566.

[12] Xu, B., Liu, J., Hou, X., Liu, B., Qiu, G., (2020). End-to-end illuminant estimation based on deep metric learning. In Proceedings of the IEEE/CVF Conference on Computer Vision and Pattern Recognition. 3616-3625.

[13] Gardner, M. A., Sunkavalli, K., Yumer, E., Shen, X., Gambaretto, E., Gagné, C., Lalonde, J. F., (2017). Learning to predict indoor illumination from a single image. arXiv preprint arXiv:1704.00090.

[14] Büyükarıkan, B., Ülker, E., (2022). Using convolutional neural network models illumination estimation according to light colors. Optik. 271:170058.

[15] Dong, K., Zhou, C., Ruan, Y., Li, Y., (2020, December). MobileNetV2 model for image classification. In 2020 2nd International Conference on Information Technology and Computer Application (ITCA). 476-480. IEEE.

[16] Kim, J., Zeng, H., Ghadiyaram, D., Lee, S., Zhang, L., Bovik, A. C., (2017). Deep convolutional neural models for picture-quality prediction: Challenges and solutions to data-driven image quality assessment. IEEE Signal processing magazine. 34(6): 130-141.

[17] Nguyen, T. S., Stueker, S., Niehues, J., & Waibel, A. (2020, May). Improving sequence-to-sequence speech recognition training with on-the-fly data augmentation. In ICASSP 2020-2020 IEEE International Conference on Acoustics, Speech and Signal Processing (ICASSP) (pp. 7689-7693). IEEE.

Kastamonu University
Journal of Engineering and Sciences
e-ISSN 2667-8209
http://dergipark.gov.tr/kastamonujes

Evaluation of the Electrochemical Behavior of NADH in the Produced Gold Nanoelectrodes

Tuğba Kır[a], Ebru Gökmeşe*[b], Faruk Gökmeşe [b]

[a] 1Department of Chemistry, Graduate School, Hitit University, Çorum, Türkiye
[b] Department of Chemistry, Faculty of Engineering and Natural Sciences, Hitit University, Çorum, Türkiye
***Corresponding Author:** ebrugokmese@hitit.edu.tr

Received: **December 01, 2025** ◆ Accepted: **June 19, 2026** ◆ Published Online: **June 24, 2026**

Abstract: In this study, gold nanoelectrodes were fabricated using a laser-based micropipette puller method and employed for investigating the nanoelectrochemical behavior of nicotinamide adenine dinucleotide (NADH). Gold wires embedded in borosilicate capillaries were subjected to thinning, sealing, and pulling processes, followed by polishing and thermal annealing to obtain reproducible nanoelectrode surfaces. The produced nanoelectrodes were characterized electrochemically by cyclic voltammetry (CV) using ferrocene as a redox mediator in acetonitrile containing 0.05 M tetrabutylammonium tetrafluoroborate (TBATFB). The average radius of the fabricated nanoelectrodes was calculated as 118.54±51.53 nm at a 95% confidence interval. The electrochemical oxidation behavior of NADH was examined in phosphate buffer solution (pH 7) containing KCl as supporting electrolyte using cyclic voltammetry and square wave voltammetry (SWV). Optimization studies were performed by varying frequency and amplitude parameters to obtain the best analytical response. The concentration–current relationship was investigated in the range of 1–4 mM NADH, and a linear relationship was obtained with a correlation coefficient of R^2=0.9954. The nanoelectrodes exhibited stable and symmetrical voltammetric responses, while increased supporting electrolyte concentration improved steady-state electrochemical behavior. The findings demonstrate that laser-fabricated gold nanoelectrodes provide a promising platform for rapid and sensitive electrochemical investigation of NADH. Due to their nanoscale dimensions and favorable mass-transfer characteristics, the produced nanoelectrodes may have potential applications in biomolecule sensing and intracellular electrochemical measurements.

Keywords: Gold Nanoelectrode, NADH, Cyclic Voltammetry, Square Wave Voltammetry

Üretilen Altın Nanoelektrotlarda NADH'nin Elektrokimyasal Davranışının Değerlendirilmesi

Öz: Bu çalışmada, lazer bazlı mikropipet çekici yöntemi kullanılarak altın nanoelektrotlar üretildi ve nikotinamid adenin dinükleotidin (NADH) nanoelektrokimyasal davranışını araştırmak için kullanıldı. Borosilikat kılcal damarlarına gömülü altın teller, tekrarlanabilir nanoelektrot yüzeyleri elde etmek için inceltme, kapatma ve çekme işlemlerine tabi tutuldu, ardından cilalama ve termal tavlama yapıldı. Üretilen nanoelektrotlar, 0,05 M tetrabutilamonyum tetrafloroborat (TBATFB) içeren asetonitril içerisinde redoks aracısı olarak ferrosen kullanılarak siklik voltametri (CV) ile elektrokimyasal olarak karakterize edildi. Üretilen nanoelektrotların ortalama yarıçapı %95 güven aralığında 118,54±51,53 nm olarak hesaplandı. NADH'nin elektrokimyasal oksidasyon davranışı, destekleyici elektrolit olarak KCl içeren fosfat tampon çözeltisinde (pH 7) siklik voltametri ve kare dalga voltametri (SWV) kullanılarak incelenmiştir. En iyi analitik cevabı elde etmek için frekans ve genlik parametreleri değiştirilerek optimizasyon çalışmaları yapıldı. Konsantrasyon-akım ilişkisi 1–4 mM NADH aralığında araştırıldı ve R^2=0,9954 korelasyon katsayısı ile doğrusal bir ilişki elde edildi. Nanoelektrotlar kararlı ve simetrik voltametrik tepkiler sergilerken, artan destekleyici elektrolit konsantrasyonu kararlı durum elektrokimyasal davranışını iyileştirmiştir. Bulgular, lazerle üretilen altın nanoelektrotların, NADH'nin hızlı ve hassas elektrokimyasal araştırması için umut verici bir platform sağladığını göstermektedir. Nano ölçekli boyutları ve uygun kütle transfer özellikleri nedeniyle üretilen nanoelektrotlar, biyomolekül algılama ve hücre içi elektrokimyasal ölçümlerde potansiyel uygulamalara sahip olabilir.

Anahtar Kelimeler: Altın Nanoelektrot, NADH, Dönüşümlü Voltametri, Kare Dalga Voltametrisi

1. Introduction

In this study, the nanoelectrochemical behavior of nicotinamide adenine dinucleotide (NADH) was investigated using electroanalytical techniques. Nicotinamide adenine dinucleotide exists in two interconvertible forms: the oxidized form (NAD^+) and the reduced form (NADH). NAD^+ functions as an electron acceptor in metabolic redox reactions, whereas NADH acts as an electron donor by carrying reducing equivalents between biochemical reactions. This coenzyme system plays a crucial role in cellular energy metabolism and ATP production. As one of the major electron carriers involved in the oxidation of fuel molecules, NADH has attracted considerable attention in electrochemical studies. [1].

NADH is frequently used in the conversion of chemical energy into electrical energy in biofuel cells. Additionally, biosensors have been developed using NAD+-dependent biocatalysts. For this purpose, redox conversion of the NAD+/NADH couple was used. Due to these important properties, studies on the electrochemical oxidation of NADH have attracted great attention [2].

Voltammetric use of micrometer-sized working electrodes, generally 1-25 microns in diameter, started in the 1980s and has become one of the important research areas in electrochemistry [3]. The main reason for using ultramicroelectrodes and smaller sized electrodes is increased mass transfer. As the electrode size decreases, multidirectional diffusion becomes dominant and thus faster mass transfer occurs [4]. Nanoscale electrochemistry is crucial to modern electrochemical science as well as many important research areas such as energy conversion and storage, catalysis, sensor development and environmental science. Nanoscale electrochemical studies have provided reliable information that cannot be achieved using the traditional method [5].

Enzymes are very powerful catalysts and play a role in many reactions such as oxidation-reduction reactions, simple electron transfer reactions, and displacement reactions in most living cells. Some redox enzymes require a small molecule called a coenzyme to be active. Nicotinamide adenine dinucleotide (NAD+) and nicotinamide adenine dinucleotide phosphate (NADP), known as pyridine nucleotides, are found in all living cells. These are coenzymes required to catalyze oxidation-reduction reactions [6].

NADPH works with enzymes that catalyze anabolic reactions by donating electrons necessary to synthesize energy-rich biological molecules. NADH plays an important role as an intermediate product in the formation of adenosine triphosphate (ATP), which occurs by oxidation of food substances in the mitochondria of the cell. NADH repairs damaged cells and DNA, is a powerful antioxidant, and has the ability to stimulate adrenaline and dopamine. Nanoelectrodes can be defined as electrodes of critical size on the order of nanometers. A microelectrode or ultramicroelectrode can be viewed as any electrode smaller than the size of the diffusion layer formed in an experiment in which the current value given by an electrode with a radius of around 25 μm is obtained [7].

One of the main driving forces for the development of nanoelectrodes has been to obtain electrodes with critical dimensions at the molecular size level. The main issues currently faced in the development of nanoelectrodes with nanoelectrodes are the preparation of devices and understanding their electrochemical performance. The use of micrometer-sized working electrodes, generally 1-25 microns in diameter, with voltammetric methods started in the 1980s and has become one of the important research areas in electrochemistry [8]. Electrochemical studies performed with nanoelectrodes and nanoelectrode groups are important in terms of characterization and application area.

Electrochemical measurement is performed to evaluate the dimensions of the produced nanoelectrodes. The signal obtained as a result of the measurement gives information about the diameter of the electrode. Due to the small size of the nanoelectrodes, three-dimensional diffusion is observed and steady-state voltammograms are obtained in a sigmoidal manner. The shape of the voltammogram is independent of the geometry of the nanoelectrode. Often a critical parameter, such as the disk diameter, provides a suitable model of the steady-state current [9].

2. Material and Method

Reagent

The nanoelectrochemical behavior of nicotinamide adenine dinucleotide in its reduced form (NADH) was investigated in this study. NADH is the reduced form of NAD^+ and plays an essential role in biological redox reactions and cellular energy metabolism (Figure 1).

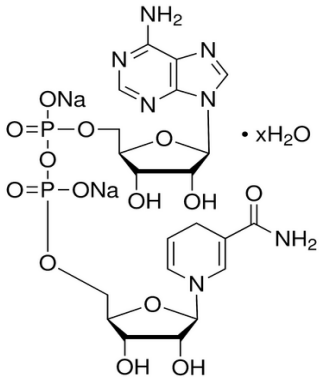

Figure 1. β-Nicotinamide Adenine Dinucleotide, reduced disodium salt (β-NADH)

Nicotinamide adenine dinucleotide (NAD+) is an important coenzyme found in cells. It plays a role in transferring the reduction potential between molecules by carrying electrons. NADH is the reduced form of NAD+ [6]. The NAD^+ molecule is composed of two nucleotides linked by phosphate groups. One nucleotide contains adenine attached to a ribose sugar, whereas the other contains a nicotinamide ring attached to another ribose sugar. These two ribose units are connected through phosphate groups. While adenine nucleotide is bonded to the first carbon atom of one of the ribose rings in the structure, nicotinamide nucleotide is bonded to the carbon atom of the other [10].

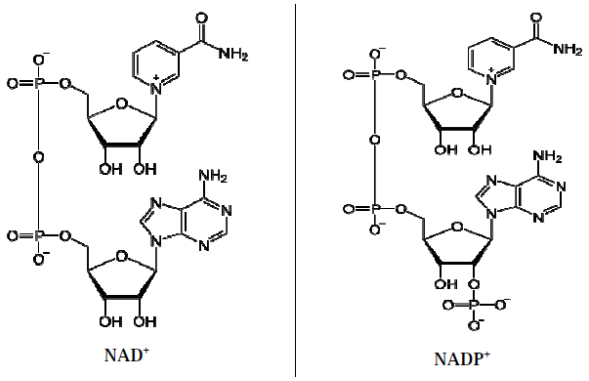

Figure 2. Structure of NAD+ and NADP+

0.05 M Tetrabutylammonium tetrafluoroborate (TBATFB) (Aldrich, 99.9%) was prepared in acetonitrile (Merck, 99.9%) solution and used as the supporting electrolyte for 1×10^{-3} M Ferrocene (Aldrich, 98%) solution. Nicotinamide adenine dinucleotide disodium salt was purchased from Sigma. For a 5×10^{-3} M stock NADH solution, it was prepared as a supporting electrolyte in phosphate buffer (Na_2HPO_4 / $NaH_2PO_4.2H_2O$) containing 0.1 M KCl at pH 7. To examine the nanoelectrochemical behavior of NADH, nanoelectrodes produced by placing a 0.025 mm diameter gold wire into borosilicate capillaries (1 mm O.D. 0.58 mm I.D) with a Sutter P-2000 laser-based micropipette puller were used. Nanoelectrodes were polished on a BV-10 micropipette polishing device. Microscope images of the electrodes were taken.

Sutter P-2000 Laser Based Micropipette Puller

P-2000 micropipette pullers represent significant advances in micropipette manufacturing, optical fiber probe and nanospray tip technology. P-2000 conventional pull devices integrate with a laser-based CO_2 heat source. Quartz provides superior material properties for a variety of research applications. Quartz is stronger than other glasses and can facilitate penetration through hard tissues [11]. This normally breaks traditional straws. Users find that quartz is the lowest noise glass available for applications requiring low noise glass [12]. Quartz glasses do not contain any metals used in traditional glasses [13].

BV-10 Micropipette Polishing Device

Distinguished and easy to use, the BV-10 is a polishing device that offers precise bevelling of micropipette tips between 0.1-100 μM. The unique sanding plate driving system vibrates freely for greater control of the polishing process. Polishing can be achieved very quickly.

Electrochemical Devices

Electrochemical studies were performed using cyclic voltammetry (CV) and square wave voltammetry (SWV) techniques on the CH Instruments Model 660C Electrochemical Analyzer. Gold nanoelectrodes with different radii were used as the working

electrode, and Ag wire was used as the semi-reference electrode. A sonicator was used to clean the normal-sized gold electrode and gold nanoelectrode and to prepare the solution. Necessary pH measurements were made with a Mettler Toledo brand pH meter calibrated with standard solutions at pH=4.40, pH=7 and pH=10.01 at 25 °C.

Method

Commercially available gold wire with a diameter of 25 μm was placed in a borosilicate glass capillary tube with an inner diameter of 0.58 mm and thinned in a laser drawing device. Studies were carried out with the values obtained after optimization of the terms heat, filament, velocity, delay, and pull, which are the parameters of the device (550, 4, 30, 150, 0, respectively). By checking under the microscope, the gold wire inside was positioned exactly in the middle.

Then, the capillary tube containing the gold wire, which was properly thinned, was placed in the laser drawing device and fused. Heat (300), filament (4), velocity (15), delay (120), and pull (0) parameters were optimized and used for fusing. Before the drawing process, the fused capillary tube and gold wire were placed in the laser drawing device; Optimization was made to include heat (400), filament (3), velocity (10), delay (120), pull (100). Two gold nanoelectrodes were obtained from a capillary tube. The nanoelectrodes, controlled under a microscope, were polished on 0.05 μm alumina polishing paper in a video-microscopic polishing device at a constant rotation speed for 15 minutes. The prepared nanoelectrodes were subjected to annealing in a muffle furnace at a temperature of approximately 150 ºC for at least 24 hours. The production method of gold nanoelectrodes using a laser drawing device is shown in Figure 3.

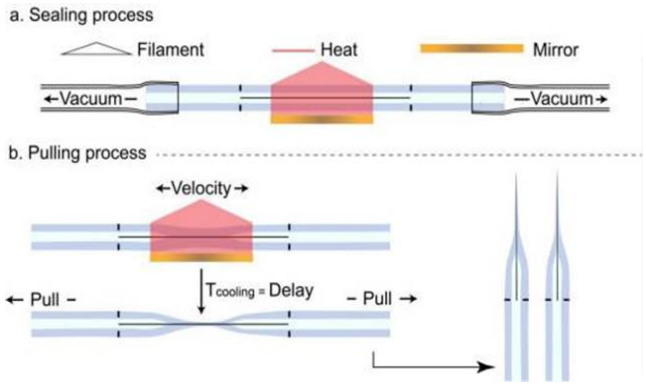

Figure 3. Schematic representation of gold nanoelectrode fabrication using a Sutter P2000 laser puller. The production stages consist of thinning, sealing and pulling processes respectively [14]

The cyclic voltammetry technique was used to calculate the approximate radius sizes of the gold nanoelectrodes produced and whose surfaces were polished. In this study, 1×10^{-3}M ferrocene solution prepared in acetonitrile was used as mediator. With the help of the shape and current values of the voltammograms obtained using ferrocene and gold nanoelectrodes, information was obtained about the smoothness and radius of the electrode's surface.

3. Result

Optical microscope results of gold nanoelectrodes

After the commercially available gold wire with a diameter of 25 μm was placed in a borosilicate glass capillary tube with an inner diameter of 0.58 mm, two gold nanoelectrodes were obtained from the capillary tube, which was subjected to thinning, fusing and drawing processes. Microscope images of nanoelectrodes are given in Figure 4.

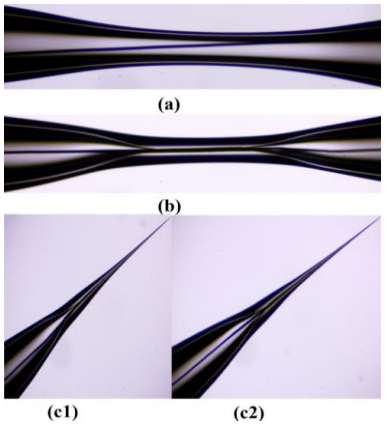

Figure 4. Nanoelectrodes obtained as a result of (a) Thinning, (b) Fusing, (c1, c2) Drawing process

Cyclic voltammetry results at normal-sized gold electrode

The oxidation of NADH in a 0.5×10^{-3} M solution on the gold electrode surface in phosphate buffer (pH=7) containing 0.1 M KCl as a supporting electrolyte was examined (Figure 5).

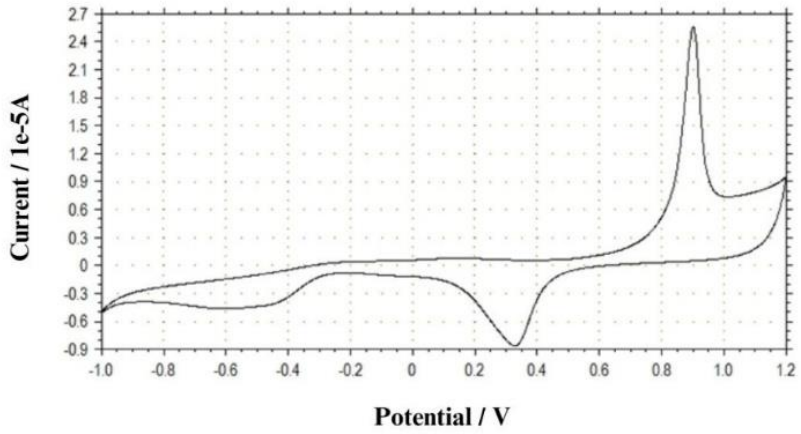

Figure 5. Voltammogram of 0.5×10^{-3} M NADH taken in pH=7 phosphate buffer containing 0.1 M KCl and normal size gold electrode *v*:0.05 V/s (vs. Pt)

Characterization of gold nanoelectrodes by cyclic voltammetry

The peak current at the gold nanoelectrode was recorded by cyclic voltammetry at a constant scanning speed in the solution of 1×10^{-3} M ferrocene, which was used as a standard reference, in acetonitrile and 0.05 M TBATFB support electrolyte (Figure 6).

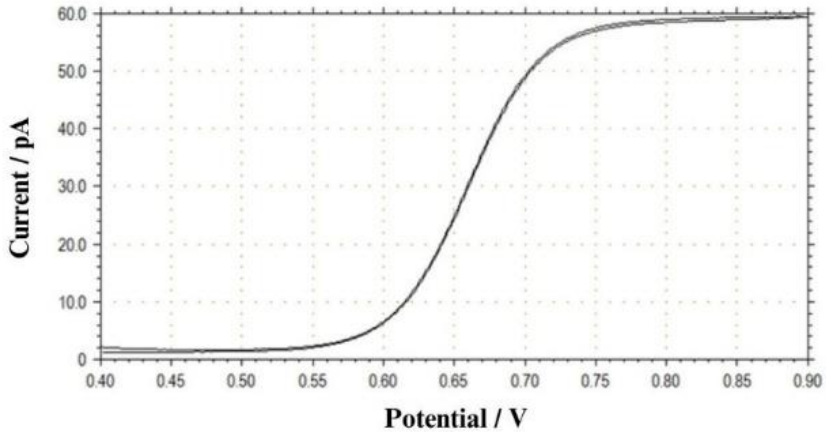

Figure 6. Voltammogram given by 1×10^{-3} M Ferrocene molecule in 0.05 M TBATFB *v*:0.01V/s (vs. Ag) (radius: 64.68 nm)

Radius calculations of gold nanoelectrodes

In calculating nanoelectrode radii, the equation giving the steady-state current used for ultramicroelectrodes was used [15].

$$\boldsymbol{i = 4nFDCr} \qquad (\mathbf{1})$$

In Equation 1, i (A) is the current, n (mole-/mol) is the number of electrodes transferred, F (C/mole-) is the Faraday constant, D (cm^2/s) is the diffusion coefficient, C (mol/cm^3) is the concentration, r (cm) is the electrode size. Steady-state current measurements were taken in 1×10^{-3} M ferrocene solution in 0.05 M TBATFB supporting electrolyte environment. The resulting steady-state currents were substituted in Equation 1 and the radius value of the electrode was calculated. The electrode radius calculated by taking the number of transferred electrons as n=1 diffusion coefficient, $D=2.64\times10^{-5}$ cm^2/s and Faraday constant as 96500 C/mole- was converted to nanometers.

The average currents and average radii obtained for the eight different nanoelectrodes produced are given in Table 1.

Table 1. Average radii of gold nanoelectrodes with 95% confidence interval

Electrode number	Average current/pA	Average Radius / nm	Deviation
1	30.50	29.93	88.61
2	88.16	86.53	32.01
3	265.33	260.57	142.03
4	193.67	190.07	71.53
5	85.50	83.91	34.63
6	65.90	64.68	53.86
7	133.50	131.02	12.48
8	103.50	101.58	16.96
Total	966.06	948.29	
N	8	8	
Average	120.76	118.54	56.51
Standard Deviation	75.72	74.36	
Confidence interval (%95)	120.76±52.47	118.54±51.53	

As seen in Table 1, the average radius at the 95% confidence interval was found to be 118.54±51.53 nm. Current measurements are the average of three replicate experiments.

Alternating voltammetry and square wave voltammetry results of NADH in gold nanoelectrode.

The voltammogram obtained using cyclic voltammetry and gold nanoelectrode in 0.1 M KCl environment is given in Figure 7.

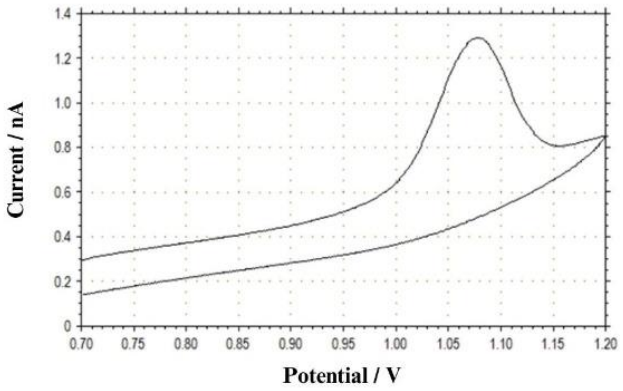

Figure 7. Voltammogram of 0.25×10^{-3} M NADH taken in pH=7 phosphate buffer containing 0.1 M KCl and 83.91 nm electrode *v*:0.1 V/s (vs. Ag)

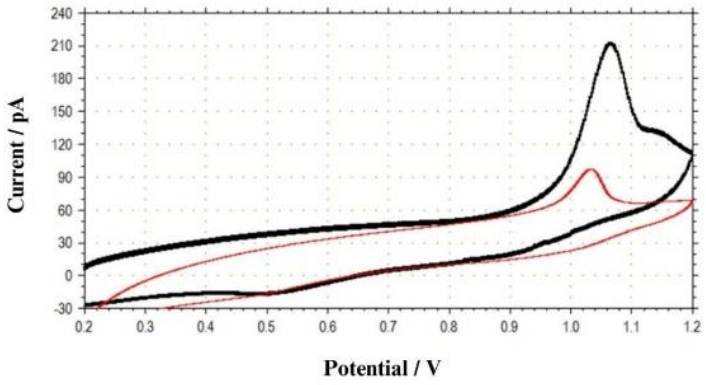

Figure 8. Voltammogram of (a) 1×10^{-3} M, (b) 0.5×10^{-3} M NADH taken in pH=7 phosphate buffer containing 0.1 M KCl and 86.53 nm electrode v:0.1 V/s (vs. Ag)

Optimization was made by measuring the peak currents at the gold nanoelectrode (radius: 101.58 nm) for 1 mM NADH solution at four different frequencies and three different amplitude values. Operating parameters frequency; 50 Hz, amplitude; After it was determined to be 0.05 V, the current-concentration relationship was examined. Currents were recorded for four different concentrations of NADH solutions prepared in pH=7 phosphate buffer at 3 M KCl concentration. The current-concentration relationship is given in Table 2.

Table 2. Current-concentration analysis

Concentration (mM)	2.5 M KCl	3 M KCl
	Current (A)	
1 mM	2.35×10^{-9}	3.82×10^{-9}
2 mM	2.93×10^{-9}	4.64×10^{-9}
3 mM	2.09×10^{-9}	4.98×10^{-9}
4 mM	3.62×10^{-9}	5.49×10^{-9}

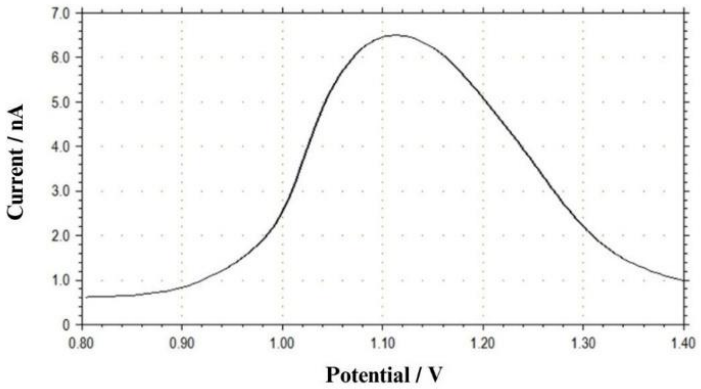

Figure 9. Square wave voltammogram of 4 mM NADH taken in pH=7 phosphate buffer containing 3 M KCl. Frequency (Hz): 50 Hz, Amplitude (V): 0.05 V (vs. Ag)

Peak currents were recorded by changing the frequency and amplitude for NADH solutions at different concentrations. Square wave voltammograms recorded for NADH at the gold nanoelectrode are smooth and symmetrical. At higher concentrations of NADH, the shape of the square wave voltammograms is smoother and the peak currents are larger (Figure 9). Voltammograms taken at two different concentrations with square wave voltammetry are seen in Figure 10.

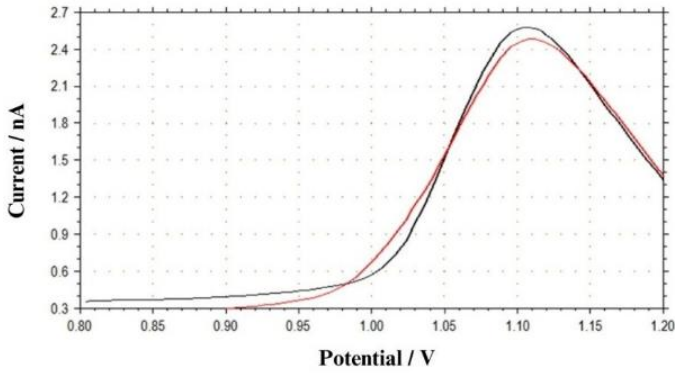

Figure 10. Square wave voltammogram of (a) 1×10^{-3} M, (b) 0.25×10^{-3} M NADH taken in pH=7 phosphate buffer containing 0.1 M KCl and 101.58 nm electrode Frequency (Hz): 50 H, Amplitude (V): 0.05 V (vs. Ag)

A linear relationship was detected when the currents measured by square wave voltammetry for 1 mM, 2 mM, 3 mM and 4 mM NADH in 2.5 M KCl and 3 M KCl medium were plotted (Figure 10). In addition, voltammograms taken with square wave voltammetry for these four different concentrations are seen in Figure 11.

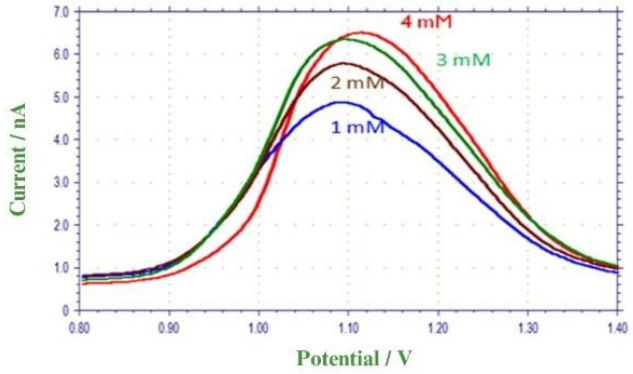

Figure 11. Square wave voltammogram of 1 mM, 2 mM, 3 mM, 4 mM NADH taken in pH=7 phosphate buffer containing 3 M KCl and at 256.812 nm electrode Frequency (Hz): 50 Hz, Amplitude (V): 0.05 V (vs. Ag)

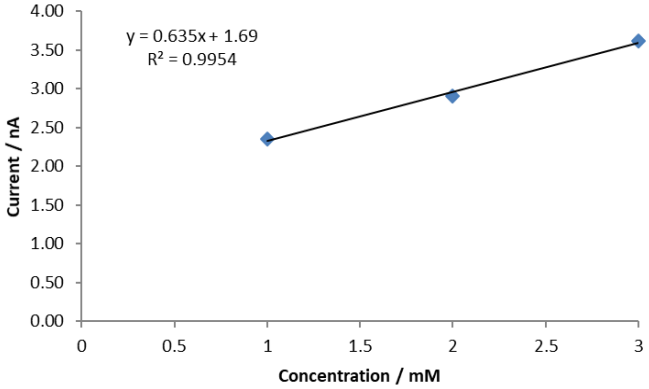

Figure 12. Current-concentration change in pH=7 phosphate buffer containing 2.5 M KCl and 256.812 nm electrode

4. Discussion

While the optimized parameters of the laser puller device affect the size of the electrode, the polishing stage affects both its size and smoothness. Gold nanoelectrodes with sizes ranging from 30 nm to 260 nm were produced with this device. As a result of the experimental studies, information about the dimensions of the successfully produced gold nanoelectrodes was obtained by cyclic voltammetry technique using Ferrocene solution as a mediator. When the gold nanoelectrode behavior of NADH was examined in phosphate buffer at pH = 7, it was seen that it was oxidized at approximately the same potential as in the normal size electrode. While a steady-state voltammogram was expected to be observed with nanoelectrodes when studied in a 0.1 M KCl environment, peaks observed with normal size electrodes were observed. This problem was resolved by increasing the support electrolyte concentration and steady-state voltammograms were obtained [16].

Experiments have been made with borosilicate and quartz glass when producing gold nanoelectrodes. While the quartz glass was in the refining stage, the gold wire melted before the glass was thinned. A proper thinning process could be achieved with borosilicate glass. For this reason, borosilicate glass was preferred in the studies.

Optimization was made by changing the frequency and amplitude for NADH solutions at different concentrations using square wave voltammetry. Current-concentration analysis was carried out under these conditions. It was observed that the shape of the square wave voltammograms was smoother and the peak currents were larger at higher concentrations of NADH. The change in the concentration of NADH directly affects cell metabolism, oxidative stress state, mitochondria function and enzymatic activities. Therefore, its rapid and sensitive measurement is valuable for biological research [17]. With electrochemical determination methods, detection can be made at lower limits than other methods. Especially with nano electrodes, measurements can be made even inside the cell. Electrochemical studies for NADH using modified electrodes and nanomaterials containing Au nanoparticles are quite common. Gold nanoparticle (AuNP)/metal nanoparticles are frequently used because they provide conductivity and electrocatalysis [18].

In principle, as the electrode size decreases from micrometers to nanometers, it becomes possible to examine faster electrochemical and chemical reactions. Because electron transfer processes are limited to mass transfer to the electron surface of the reactant under conditions of very high speed mass transfer [4]. It is easy to obtain steady-state current with nanoelectrodes, measurement is possible at low concentrations, and very fast electron transfers can be monitored. For this reason, nanomaterials are preferred especially in the determination of biomolecules such as NADH, dopamine, H_2O_2, and NO [19].

5. Conclusion

To further evaluate the sensing performance of the fabricated gold nanoelectrodes, the obtained electroanalytical parameters were compared with previously reported NADH sensing systems. Compared to conventional and nanomaterial-modified electrodes reported in the literature, the fabricated nanoelectrodes showed a linear response with a high correlation coefficient ($R^2 = 0.9954$) in the concentration range of 1–4 mM. Although some modified electrodes provide lower detection limits due to catalytic nanomaterials, this work demonstrates the feasibility of direct NADH detection using bare gold nanoelectrodes fabricated by the laser drawing technique, without requiring additional surface modification. Additionally, the nanoelectrode geometry may offer advantages in rapid mass transfer and future intracellular electrochemical applications.

Competing Interest / Conflict of Interest

The authors declare that they have no competing interests.

Author Contribution

We declare that all Authors equally contribute.

Acknowledgements

We would like to thank Hitit University Scientific Research Projects Coordination Office for their support to this study within the scope of project number FEF19004.15.003.

6. References

[1] Covarrubias, A.J., Perrone, R., Grozio, A., Verdin, E. (2021). NAD+ Metabolism and its Roles in Cellular Processes During Ageing. Nature Reviews|Molecular Cell Biology. 22:121-141.
[2] Immanuel,S., Sivasubramanian, R. (2020). Electrochemical Studies of NADH Oxidation on Chemically Reduced Graphene Oxide Nanosheets Modified Glassy Carbon Electrode. Materials Chemistry and Physics. 249:123015.
[3] Murray, R.W. (2008). Nanoelectrochemistry: Metal Nanoparticles, Nanoelectrodes, and Nanopores. Chemical Reviews. 108:2688-2720.
[4] Arrigan, D.W.M. (2004). Nanoelectrodes, Nanoelectrode Arrays and Their Applications. Analyst. 129:1157-1165.
[5] Hatamie, A., He, X., Zhang, X.W., Oomen, P.E., Ewing, A.G. (2023). Advances in Nano/microscale Electrochemical Sensors and Biosensors for Analysis of Single Vesicles, a Key Nanoscale Organelle in Cellular Communication. Biosensors and Bioelectronics. 220:114899.
[6] Munk, S.H.M., Maya, J.M., Rubio, A.A., Pappas, G., Mendoza, A. (2023). NAD+ Regulates Nucleotide Metabolism and Genomic DNA Replication. Nature Cell Biology. 25:1774-1786.
[7] Hyk, W., Stojek, Z. (2024). Are micro- and nanoelectrodes just smaller versions of regular electrodes? Journal of Solid State Electrochemistry. 28:1331-1339.
[8] Arrigan, D.W.M. (2008). Nanoelectrodes, Nanoelectrode Arrays and Their Applications. Analyst. 129:1157-1165.
[9] Zhang, Y., Li, D., Compton, R.G. (2022). Arsenic (III) Detection with Underpotential Deposition on Gold. Journal of Electroanalytical Chemistry. 909:116154.
[10] Munk, S. H. N., Merchut-Maya, J. M., Adelantado Rubio, A., et al. (2023). NAD^+ regulates nucleotide metabolism and genomic DNA replication. Nature Cell Biology, 25(12), 1774–1786.
[11] Munoz, J.L., Coles, J. (19879. Quartz Micropipettes for Intracellular Voltage Micro- electrodes and Ion Selective Microelectrodes. Journal of Neuroscience Methods. 22:57-64.
[12] Rae, J.L., Levis, R.A. (1992). A Method for Exceptionally Low Noise Single Channel Recordings. European Journal of Physiology - Pflügers Archiv. 420:618-620.
[13] Zuazaga, C., Steinacker, A. (1990). Patch-clamp Recording of Ion Channels: Interfering Effects of Patch Pipette Glass. News in Physiological Science. 5:155-159.
[14] Lim, K., Goines, S., Demg, M., Dick, J.E. (2023). A Troubleshooting Guide for Laser Pulling Platinum Nanoelectrodes. Analyst. 148(13):2992-3001.
[15] Cox, J., Guerette, J., Zhang, B. (2012). Steady-State Voltammetry of a Microelectrode in a Closed Bipolar Cell. Analytical Chemistry. 84(20):8797-8804.
[16] Dickinson, E.J.F., Compton, R.G. (2011). Influence of the Diffuse Double Layer on Steady-state Voltammetry. Journal of Electroanalytical Chemistry. 661:198–212.
[17] Koo, K.M., Kim, C.D., Kim, T.H. (2024). Recent Advances in Electrochemical Detection of Cell Energy Metabolism. Biosensors (Basel). 14(1):46.
[18] Sarakatsanou, C., Karastogianni, S., Girousi, S. (2023). Romising Electrode Surfaces, Modified with Nanoparticles, in the Sensitive and Selective Electroanalytical Determination of Antibiotics. Applied Science. 13(9): 5391;
[19] Lee, J.K., Suh, H.N., Yoon, S.H., Lee, K.H., Ahn, S.Y. (2022). Non-Destructive Monitoring via Electrochemical NADH Detection in Murine Cells. Biosensors (Basel) 10;12(2):107.

Kastamonu University
Journal of Engineering and Sciences
e-ISSN 2667-8209
http://dergipark.gov.tr/kastamonujes

The Role of the Insurance Sector in Climate Finance: Risk Transfer, Resilience, and Capital Allocation

Ahmet Codal *

Directorate of Climate Change, Ankara, Türkiye
***Corresponding Author:** ahmet.codal@iklim.gov.tr

Received: **April 20, 2026** ◆ Accepted: **June 10, 2026** ◆ Published Online: **June 24, 2026**

Abstract: Climate finance debates have traditionally centered on public budgets, development finance institutions, and capital markets, while the role of the insurance sector has remained comparatively underexamined in an integrated manner. Existing studies address insurance in relation to climate risk, catastrophe coverage, adaptation, investment, and financial governance; however, ~~but~~ these perspectives are seldom integrated into a unified climate finance framework. This review article examines the role of the insurance sector in climate finance through three core dimensions: risk transfer, resilience, and capital allocation. It argues that this tripartite structure captures the sector's most climate-finance-relevant functions more coherently than fragmented categorizations because it reflects insurers' role in providing financial protection against loss, shaping adaptive capacity and recovery, and directing long-term investment. The article further argues that risk pricing, modelling, and the production of climate information should not be treated as a standalone pillar, but rather as a cross-cutting function that supports and underpins all three dimensions. Reviewing the literature across climate adaptation, disaster risk finance, institutional investment, and insurance governance, the article identifies both the opportunities and structural limits of insurance-led climate finance. It concludes that the insurance sector can be understood as a strategically important but institutionally bounded actor within climate finance, especially in adaptation and resilience, whose contribution depends on supportive public policy, regulatory coordination, and layered risk-sharing systems.

Keywords: Climate Finance, Insurance Sector, Risk Transfer, Resilience, Capital Allocation

Sigorta Sektörünün İklim Finansmanındaki Rolü: Risk Transferi, Dirençlilik ve Sermaye Dağılımı

Öz: İklim finansmanı tartışmaları geleneksel olarak kamu bütçeleri, kalkınma finansmanı kuruluşları ve sermaye piyasaları etrafında şekillenmiş; buna karşılık sigorta sektörünün rolü bütüncül bir çerçevede görece daha az incelenmiştir. Mevcut çalışmalar, sigortayı iklim riski, afet teminatı, uyum, yatırım ve finansal yönetişim gibi farklı başlıklar altında incelemektedir; ancak bu yaklaşımlar çoğu zaman birleşik bir iklim finansmanı çerçevesi içinde bir araya getirilmemektedir. Bu derleme makalesi, risk transferi, dirençlilik ve sermaye tahsisi olmak üzere üç temel boyut üzerinden iklim finansmanında sigorta sektörünün rolünü incelemektedir. Çalışma, bu üçlü yapının sektörün iklim finansmanı bakımından en önemli işlevlerini parçalı sınıflandırmalara kıyasla daha tutarlı biçimde yansıttığını savunmaktadır; zira bu yapı, sigortacıların kayıplara karşı finansal koruma sağlama, uyum kapasitesi ile toparlanma süreçlerini biçimlendirme ve uzun vadeli yatırımları yönlendirme konusundaki rolünü yansıtmaktadır. Makale ayrıca, risk fiyatlaması, modelleme ve iklim bilgisinin üretilmesinin bağımsız bir sütun olarak değil, söz konusu üç boyutun tamamını destekleyen ve temellendiren kesişen bir işlev olarak değerlendirilmesi gerektiğini ileri sürmektedir. Uyum, afet risk finansmanı, kurumsal yatırım ve sigorta yönetişimi alanlarındaki literatürü gözden geçiren çalışma, sigorta temelli iklim finansmanının hem sunduğu fırsatları hem de yapısal sınırlılıklarını ortaya koymaktadır. Sonuç olarak sigorta sektörü, özellikle uyum ve dirençlilik alanlarında, iklim finansmanı içinde stratejik öneme sahip; ancak kurumsal sınırlarla çevrili bir aktör olarak konumlanmaktadır. Bu katkının etkili biçimde ortaya çıkabilmesi ise destekleyici kamu politikalarına, düzenleyici eşgüdüme ve katmanlı risk paylaşımı mekanizmalarına bağlıdır.

Anahtar Kelimeler: İklim Finansmanı, Sigorta Sektörü, Risk Transferi, Dirençlilik, Sermaye Dağılımı

1. Introduction

Climate change has become a defining challenge not only for environmental governance, but also for financial systems, fiscal stability, and development policy. Although global climate finance has expanded over the past decade, adaptation continues to receive substantially less attention and funding than mitigation, despite escalating climate vulnerability, disaster losses, and recovery needs [1]. This imbalance increasingly calls for a broader understanding of climate finance—one that goes beyond project-level investment flows and incorporates the institutions, incentives, and financial arrangements through which societies absorb, distribute, and respond to climate-related risk [2]. Such an approach is consistent with broader conceptualisations of climate finance advanced by the IPCC, which emphasise that climate finance includes not only capital flows, but also the institutional and financial arrangements shaping mitigation and adaptation outcomes [3]. Within this expanded framework, the insurance sector warrants more central analytical attention than it has typically received in mainstream climate finance debates. This relative marginalization can also be linked to broader patterns in climate change discourse, where certain actors and policy instruments are prioritized while others remain less visible [4].

Insurance plays a critical role in protecting households, firms, and governments from the financial consequences of climate-related shocks. Yet climate change is also expected to increase the frequency, severity, and correlation of weather-related losses, potentially threatening the future affordability and availability of coverage. OECD [5] explicitly notes that the future viability of insurance markets will depend heavily on stronger adaptation and risk reduction. This dual reality places the insurance sector at the heart of a growing tension within climate finance: the need to strengthen financial resilience in the face of accelerating climate risk, while recognising that market-based insurance solutions are themselves shaped and constrained by that same risk environment. As a result, the significance of insurance extends well beyond claims-paying. Insurers operate simultaneously as risk managers, loss absorbers, information producers, and long-term institutional investors, a dual role also emphasised by the Geneva Association [6]. This combination makes them relevant not only to post-disaster recovery, but also to adaptation, resilience-building, investment allocation, and the wider translation of climate risk into financially actionable signals.

The literature on insurance and climate change has grown substantially in recent years. Important contributions now exist on catastrophe insurance, disaster risk finance, climate adaptation, resilience, institutional investment, climate-risk governance, and green finance. However, these contributions remain largely dispersed across partially disconnected subfields [7]. Existing studies often analyse a specific aspect of the insurance-climate nexus—for example, catastrophe coverage, adaptation incentives, disclosure, or green investment—without fully integrating these functions into a broader climate finance perspective [7, 8]. The primary deficiency, consequently, is not in insufficient scholarship but in inadequate integration: while the significance of insurance is progressively recognized in climate-related research, it remains comparatively underexplored as the central element of a thorough climate finance analysis [9].

This article addresses that gap by examining the role of the insurance sector in climate finance through three interrelated dimensions: risk transfer, resilience, and capital allocation. The adoption of this tripartite structure is neither arbitrary nor merely descriptive. Rather, it reflects an analytical judgement that the sector's climate-finance relevance is most coherently understood through the three principal channels by which insurers contribute to the financing of climate-related outcomes. This approach is consistent with the broader literature, which views insurers as institutional investors with the ability to influence long-term capital allocation as well as actors that support resilience-building and risk management and financial protection [5, 6]. Risk transfer captures the sector's most visible and traditional function: the provision of pre-arranged financial protection, post-shock liquidity, and loss-sharing across actors, geographies, and time [5, 8]. Resilience captures the wider adaptation-related role of insurance, including the shaping of incentives for prevention, preparedness, risk reduction, and more resilient recovery [5]. Capital allocation captures the asset-side role of insurers as major institutional investors capable of influencing long-term investment flows relevant to climate mitigation, transition, and adaptation [10, 11]. Considered together, these three dimensions reveal insurers not merely as compensatory market institutions, but as multifunctional climate finance actors operating across both the liability and asset sides of the balance sheet.

The tripartite framework also clarifies a recurrent conceptual ambiguity in the literature regarding the place of risk pricing, catastrophe modelling, climate data production, scenario analysis, and information provision within the insurance–climate nexus [12]. While these functions are indispensable to understanding the sector's role, they do not constitute a separate dimension of climate finance contribution. Rather, they operate as cross-cutting informational and analytical processes that shape the three core dimensions identified here: they determine the conditions of risk transfer, influence the incentive structures associated with resilience, and inform the evaluative basis of capital allocation decisions [6, 9]. Their inclusion in the analysis is therefore necessary not as an additional pillar, but as part of the underlying architecture through which insurers engage with climate finance.

A similar distinction applies to regulation, supervision, public support, and governance. These are indispensable in determining whether and to what extent the insurance sector can contribute effectively to climate finance, but they are best understood as enabling or constraining conditions rather than as core functional dimensions of that contribution [5, 13]. This distinction is analytically important because it preserves clarity between what the insurance sector does and the institutional conditions under which it can do so. Therefore, the article views insurance as a strategically significant, institutionally mediated part of larger climate finance systems rather than as a stand-alone market solution.

Against this background, the core argument advanced here is that the insurance sector should be understood as a structurally significant, operationally diverse, but institutionally bounded actor in climate finance. Its contribution is potentially substantial—particularly in adaptation and resilience—but neither automatic nor unlimited [3, 9]. The sector's future role depends on whether risk transfer, resilience-building, and capital allocation are embedded within supportive public policy, effective regulatory coordination, layered risk-sharing arrangements, and broader climate adaptation strategies [5, 13]. The paper aims to give a more comprehensive and analytically sound explanation of how the insurance industry fits into current climate financing discussions by examining the literature through this perspective.

Figure 1 visualizes this analytical framework and clarifies how the article links the three core functions of insurance--risk transfer, resilience, and capital allocation--with the cross-cutting role of risk pricing, modelling, and climate-risk information.

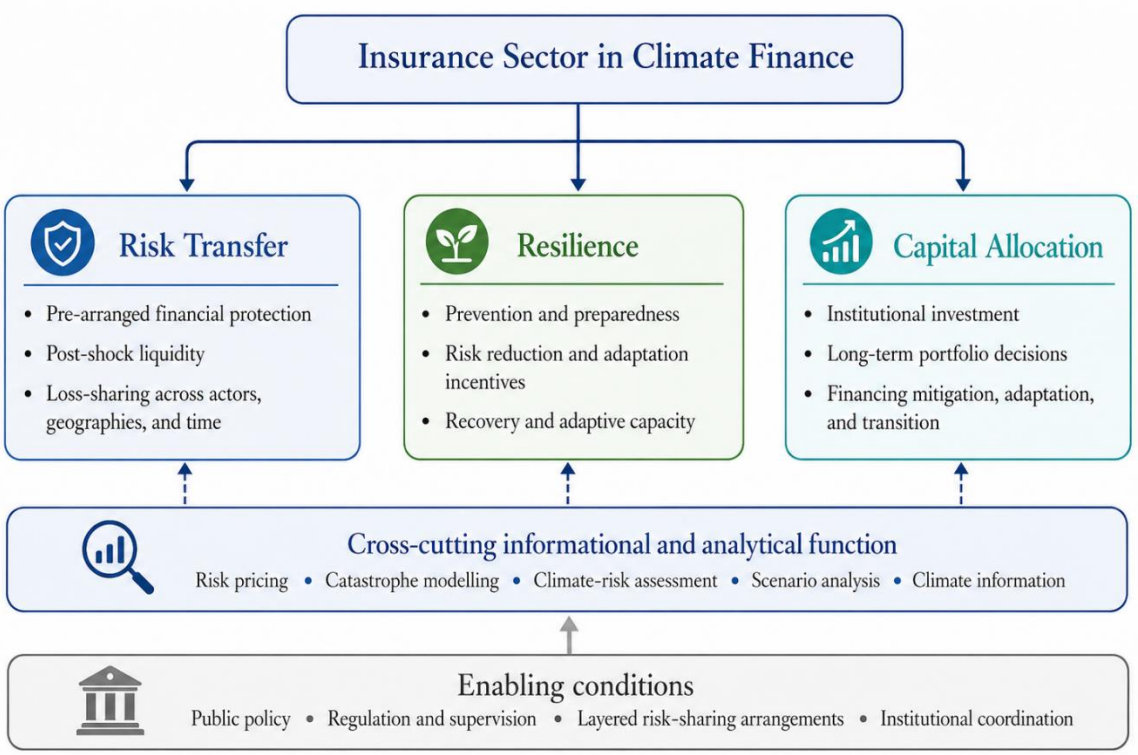

Figure 1. Conceptual Framework of the Insurance Sector in Climate Finance

2. Literature Review

The literature on climate change and insurance has expanded considerably, but it remains dispersed across several overlapping lines of inquiry. Recent studies indicate that the link between insurance and climate change now extends beyond traditional concerns regarding catastrophe coverage to encompass acute and chronic physical risks, as well as issues related to adaptation, mitigation, governance, innovation, and public awareness [9]. At the same time, this expanding body of research continues to approach the sector through relatively distinct analytical lenses such as disaster risk finance and risk transfer [8, 14], adaptation and resilient recovery [3], institutional investment [10, 11], and climate-risk governance and disclosure [6]. For example, OECD [5] conceptualizes insurance primarily as a mechanism for financial protection, risk reduction, and resilient reinstatement, while the Geneva Association [6] emphasizes insurers' dual role as risk managers and long-term institutional investors. Similarly, United Nations Environment Programme Finance Initiative (UNEP FI) [15] highlights the need to assess climate-related risks in an integrated manner across both underwriting portfolios and investment activities, pointing to the growing but still only partially consolidated treatment of insurance within broader climate-finance debates. Taken together, this literature demonstrates that insurance is no longer peripheral to climate-related research. However, it also reveals that the sector is rarely analyzed within a single, unifying climate finance framework. Therefore, the main gap is not so much in the lack of conceptual or empirical work as it is in the poor integration of these strands into a cohesive analytical explanation of how insurers contribute to climate finance.

This article responds to that fragmentation by reorganizing these dispersed strands of research into three primary categories that correspond to the insurance sector's most climate-finance relevant functions: risk transfer, resilience, and capital allocation. In doing so, it moves beyond the tendency to treat disaster risk finance, adaptation, institutional investment, and climate-risk governance as largely separate domains of inquiry, and instead brings them into a common analytical framework centered on climate finance. Although these categories do not cover every topic in the insurance-climate literature, they do identify the primary mechanisms via which insurers impact financial reactions to climate change. This structure's ability to consolidate previously separate lines of research into a more comprehensive account of the sector's role in climate financing is precisely what distinguishes it analytically.

The first category focuses on insurance as a mechanism of climate risk transfer, particularly in relation to catastrophes, disaster risk finance, and climate-related loss and damage. Nobanee and Nghiem [8] review climate catastrophe insurance as an expanding but still fragmented field, while Surminski [14] shows that insurance risk transfer can also enable climate-relevant investment by reducing uncertainty around future losses, especially in developing-country contexts. This literature increasingly emphasises that risk transfer cannot be reduced to traditional indemnity insurance alone. It includes sovereign and sub-sovereign disaster risk financing, regional risk pools, parametric insurance, microinsurance, and reinsurance-backed structures that channel rapid liquidity after shocks [16, 17]. This category also makes the point that the value of insurance is determined by how well it is integrated into larger risk management systems. Studies on integrated climate risk management and loss-and-damage governance argue that risk transfer is most effective when combined with contingency planning, risk layering, early warning, and ex ante risk reduction rather than treated as a standalone market product [5, 16, 18].

The second category addresses insurance and resilience, most often through the lens of climate adaptation. OECD [5] is especially important here in arguing that insurers can contribute not only by compensating losses, but also by encouraging prevention, preparedness, resilient reinstatement, and improved climate-risk analytics. This strand of literature is especially important because it repositions insurance within adaptation finance and resilience-building rather than treating it solely as a post-disaster financing mechanism. It also emphasizes the essential conflict that insurance is frequently most socially helpful in precisely those settings where commercial viability is weakest due to price limits, limited penetration, and high-risk exposure [5, 8].

The third category concerns capital allocation, especially the role of insurers as major institutional investors. This literature matters because insurers manage substantial long-term portfolios and therefore participate in climate finance not only on the liability side, but also on the asset side of their balance sheets. Golnaraghi [10] highlights this dual role of insurers as both risk managers and investors. In principle, this positions insurers as potentially important actors in financing renewable energy, green bonds, climate-resilient infrastructure, and other transition or adaptation related investments. At the same time, the literature is cautious about assuming that the existence of long-term capital automatically translates into climate-aligned investment outcomes. Ameli et al. [11] show that disclosure alone is insufficient to redirect institutional investor finance toward public-interest climate goals, while Jakubik and Uguz [19] find that green bond commitments by European insurers did not consistently produce strong positive market effects.

Across these three categories, a further body of work focuses on climate-risk governance, modelling, and information production. This includes research on catastrophe modelling, scenario analysis, disclosures, climate-risk data, and underwriting methodologies. Geneva Association [6] is central here because it demonstrates how insurers integrate climate-risk assessment across both the liability and asset sides of the balance sheet. These contributions are analytically indispensable because they show how insurers make climate risk financially legible. Yet their role is best understood as cross-cutting. Risk transfer depends on how climate risks are measured and priced; resilience depends on how climate information shapes incentives and adaptation decisions; and capital allocation depends on how future risk is interpreted within investment strategies [6, 9]. For this reason, the present article does not treat risk pricing and modelling as a standalone fourth pillar. Doing so would risk reproducing the fragmentation that the article seeks to overcome. Instead, these functions are conceptualised as the informational and analytical infrastructure underpinning all three core dimensions.

Taken together, the literature reveals that the insurance sector is already embedded in climate-related study, yet rarely as the major topic of an integrated climate finance analysis. Risk transfer, resilience, and capital allocation are frequently discussed, but seldom brought together as the defining modes through which insurers contribute to climate finance. This article develops that synthesis and, in doing so, seeks to clarify both the opportunities and the structural limits of insurance-led climate finance.

3. Material and Method

This article employs a narrative review technique based on a thematic and functionally oriented analytical framework. Its goal is not to create a bibliometric map or a narrowly focused screening exercise, but rather to synthesize the most relevant academic and institutional literature on the three main dimensions through which insurance enters climate finance: risk transfer, resilience, and capital allocation. A narrative review is particularly appropriate here because the central question is not simply whether insurance matters in the context of climate change, but how it matters, through which mechanisms, and under what institutional conditions [5, 9].

The literature was selected according to thematic and functional relevance to the insurance–climate finance nexus rather than through a systematic or bibliometric screening protocol. Priority was given was given to works that address at least one of the three core analytical dimensions examined here -risk transfer, resilience, and capital allocation- or the cross-cutting issues of climate-risk modelling, pricing, governance, regulation, and insurance-sector investment. Peer-reviewed academic studies were included to capture scholarly debates and empirical findings, while institutional reports from organisations such as the OECD, IPCC, UNEP FI, and the Geneva Association were also included because they provide policy-relevant frameworks, supervisory perspectives, market data, and practitioner-oriented analyses that are central to understanding the insurance sector's role in climate finance. This combination of academic and institutional sources is therefore consistent with the article's narrative review approach, which aims to integrate dispersed strands of literature into a coherent conceptual framework.

This framing is also consistent with broader understandings of climate finance that go beyond direct capital flows and instead emphasise the institutions, incentives, and financial arrangements shaping mitigation and adaptation outcomes [3]. Under such

a perspective, insurers assist not just by transferring money directly, but also by organizing financial protection, setting behavioral incentives, affecting recovery trajectories, and generating knowledge that makes climate risk actionable in economic and financial decision-making [6]. Insurance thus belongs within climate finance not merely because it pays claims or invests assets, but because it plays a constitutive role in how societies organise financial responses to climate-related uncertainty.

The tripartite structure adopted in this article is intended to reflect the insurance sector's contribution to climate finance in an analytically concise and conceptually robust manner. Risk transfer represents the sector's core liability-side role in absorbing, pooling, and redistributing climate-related losses through insurance, reinsurance, catastrophe mechanisms, and associated instruments [5, 8]. Resilience captures insurance's broader adaptation-related function by incorporating prevention, preparedness, risk reduction, and recovery capacity [5]. Capital allocation reflects insurers' asset-side importance as large institutional investors whose portfolio decisions shape the direction of long-term finance [10, 11]. Taken together, these three dimensions reveal that the insurance sector participates in climate finance not through a single mechanism, but through a combination of compensatory, adaptive, and allocative roles.

This structure also helps to avoid a common tendency in the literature to confuse functional contributions with enabling conditions or cross-cutting capacities. As noted above, modelling, pricing, climate data production, and scenario analysis are central to the insurance-climate nexus, but they do not constitute separate channels of contribution in the same way that risk transfer, resilience, and capital allocation do. They are better understood as forms of analytical infrastructure that operate across all three dimensions [6, 9]. Likewise, governance and regulation shape the effectiveness, scope, and distributional consequences of insurance-based climate finance, but they do not define its core functions [5, 13]. The present framework is designed precisely to retain these distinctions while integrating the relevant strands of literature into a coherent whole.

The Role of the Insurance Sector in Climate Finance

Risk Transfer

Risk transfer is the most visible and historically established way in which the insurance sector contributes to climate finance. Through insurance, reinsurance, catastrophe pools, and other forms of pre-arranged protection, climate-related losses can be spread across policyholders, geographies, time horizons, and in some cases capital-market actors. This redistribution reduces the immediate burden of shocks on households, firms, and governments, and limits the extent to which climate disasters translate into abrupt fiscal stress, interrupted recovery, and long-lasting macroeconomic disruption [5, 8]. In climate finance terms, the significance of risk transfer lies not simply in compensating losses after they occur, but in creating an organised financial architecture through which climate shocks become more manageable, more predictable, and more rapidly financeable [16].

The literature also demonstrates that risk transfer is a multi-layered set of arrangements rather than a single tool. At household and firm level, protection may take the form of microinsurance or conventional property cover; at meso and sovereign levels it often involves reinsurance-backed programmes, regional pools, or public-private facilities; and at the macro end it may extend to catastrophe bonds and other insurance-linked securities that shift part of climate-related disaster risk to capital markets [14, 17]. This differentiation matters analytically because the climate-finance contribution of insurance depends not only on whether coverage exists, but on who is covered, which layer of loss is transferred, and how rapidly liquidity can be mobilised after an event. The risk-layering literature is especially important here: lower-severity and more frequent losses are often better addressed through prevention, retention, or contingency funding, whereas lower-frequency and higher-impact losses are more suitable for transfer through insurance and reinsurance [16]. Well-designed risk transfer can therefore reduce reconstruction delays, smooth fiscal shocks, and limit emergency reallocations from already constrained public budgets, especially when embedded in broader disaster risk financing strategies [5, 17].

A further insight from the recent literature is that product design shapes the developmental value of risk transfer. Indemnity insurance can track realised losses more closely but may involve costly and slower loss adjustment, whereas parametric and index-based instruments can pay out rapidly on the basis of pre-defined triggers but introduce basis risk, the possibility that the payout diverges from actual loss [18]. This trade-off is particularly important in climate-vulnerable contexts where speed of disbursement is critical for emergency response, yet legitimacy and trust depend on whether instruments match experienced losses. For that reason, several studies stress that climate risk transfer should be evaluated not only by premium volume or coverage rates, but also by trigger design, transparency, data quality, and its integration with contingency planning, early warning, and social protection systems [17, 18]. Recent scholarship further strengthens this interpretation by showing that higher levels of insurance coverage are associated with less severe macroeconomic consequences following climate-related catastrophes. Giuzio et al. [20] demonstrate that declining insurance coverage under stronger warming scenarios could amplify macroeconomic losses. This suggests that insurance should not be understood merely as a compensatory instrument, but also as a mechanism of macro-financial stabilisation under climate stress. At the same time, slower-onset processes such as sea-level rise, salinisation, and desertification reveal that traditional non-life contracts are often poorly matched to gradual and cumulative forms of loss, which may require multi-year structures, modified triggers, or complementary public financing arrangements rather than standard short-term coverage alone [18].

However, it is important to be aware of the limits of risk transfer. Given climate change's potential to increase the frequency and severity of losses, insurability may be strained and premiums may rise. As risks become more severe and less diversifiable, some forms of coverage may become increasingly unaffordable or unavailable. OECD [5] explicitly warns that climate change may reduce the future availability of affordable insurance unless adaptation and risk reduction improve in parallel. The literature on loss and damage and inclusive insurance further shows that pure market provision is often weakest where vulnerability is highest, which is why public support, premium subsidies, contingency funds, and layered public-private arrangements are frequently needed to reach low-income groups and climate-exposed sectors [14, 17, 18]. Recent academic studies add a further prudential dimension to this discussion: as physical, transition, and liability risks are increasingly reflected in insurers' balance sheets, supervisory authorities are placing growing emphasis on firms' integration of climate risk into enterprise risk management, scenario analysis, and their own risk and solvency assessment; however, modelling approaches remain inconsistent and are still most developed in the area of physical risk [21]. Risk transfer alone therefore cannot solve the climate finance challenge. Its continued effectiveness depends on parallel investments in adaptation, risk reduction, and institutional arrangements that preserve both affordability and legitimacy in an era of escalating climate exposure [5, 16].

Resilience

The second major contribution of the insurance sector lies in resilience-building. Although insurance is often framed as an ex-post compensation mechanism, the literature increasingly shows that its climate-finance relevance is equally tied to what it does ex ante. In resilience terms, insurance matters because it can help systems absorb shocks, recover more quickly, preserve core functions, and reduce future vulnerability; in adaptation terms, it helps translate climate risk into planning, pricing, and investment decisions before losses occur [22]. This is particularly important at a time when adaptation finance remains comparatively underdeveloped relative to mitigation finance, even though present-day climate losses are already affecting balance sheets, fiscal stability, and development outcomes [5].

Insurance promotes resilience through a variety of interconnected channels. Le Quesne et al. [16] explicitly notes that insurance against extreme weather events can increase resilience not only through compensation, but also by signalling risk through premiums and deductibles and by encouraging risk management. OECD [5] deepens this argument by identifying four areas where insurers support adaptation: climate-conditioned risk analytics, the communication of risk information, incentives for prevention and adaptation, and more resilient reinstatement after claims. Jarzabkowski et al. [23] extend the same logic by arguing that insurance is most effective when embedded in broader adaptation strategies that improve risk literacy, align public policy, and strengthen Build Back Better practices. Under this logic, insurance becomes part of adaptation finance even when it does not directly fund a formally labelled adaptation project.

The resilience literature also highlights the growing importance of product innovation. ClimateWise [24] argues that climate-ready insurance products are those that incorporate resilience and adaptation objectives into the business models and operations of policyholders. The same logic appears in urban resilience debates. Climate Policy Initiative [1] describes insurance as a crucial tool for building fiscal and physical resilience in cities, not only because city governments can purchase coverage, but also because they can use insurance within broader planning, risk governance, and investment strategies. Parametric solutions further expand this resilience toolkit by providing rapid liquidity after predefined climate triggers are met, which can be especially valuable for agriculture, local public services, and climate-vulnerable communities; however, their effectiveness depends on careful product design, management of basis risk, and, in many contexts, hybrid combinations with traditional cover [23].

Another way to boost resilience is to link adaptation investment to better financial outcomes. Climate adaptation and resilience investments can reduce expected losses and strengthen the long-term sustainability of insurance markets and underwriting capacity [13]. Adaptation is also increasingly framed not only as a loss-reduction mechanism but as a strategic investment process capable of generating broader economic and financial returns [13]. In this sense, insurance contributes to resilience not only by financing recovery, but also by helping translate physical climate risk into signals that can preserve asset values, lower volatility, support creditworthiness, and improve long-term insurability.

However, the resilience function of insurance illustrates one of the sector's key structural paradoxes. Insurance is frequently most socially necessary in situations characterized by high vulnerability, low income, limited information, and insufficient public protection. These are also the conditions under which private insurance markets are least likely to function efficiently on a commercial basis. Affordability limits, poor penetration rates, weak technical capacity, and significant risk exposure might result in protection gaps precisely where resilience needs are most needed [1, 5]. Recent literature also warns that systemic and cumulative shocks—including disruptions spreading through supply chains and infrastructure networks—are challenging traditional assumptions regarding independent losses and short insurance cycles, making it difficult to ensure long-term resilience using traditional market products alone [25]. This is why the resilience literature consistently points toward layered risk financing, public-private partnerships, premium support, resilience bonds, and closer integration between insurance systems, supervisory frameworks, and adaptation planning [26, 27].

Finally, resilience should also be understood as an internal characteristic of insurers themselves. Climate risk affects pricing, solvency, operational efficiency, and business models, which means that the sector's ability to support societal resilience depends partly on its own institutional resilience. Recent empirical work from China finds that physical climate risk can reduce insurers' operational efficiency, while resilient infrastructure and insurance technology can mitigate adverse effects and support

gradual transformation [28]. Complementing this, qualitative evidence from senior industry experts shows that insurers are responding through product portfolio changes, environmentally oriented investment strategies, and stronger collaboration with regulators and public authorities [29]. The resilience role of insurance is therefore two-sided: insurers support the resilience of others, but must also adapt their own governance, analytics, and operating models if they are to remain credible climate-finance actors over the long run.

Capital Allocation

A third and often less appreciated dimension of the insurance sector's climate-finance relevance is capital allocation. Insurers are among the world's largest institutional investors, managing significant portfolios against long-term obligations, giving them an asset-side position in climate finance that is equal to their liability-side role in risk transfer. However, this position is structurally mediated by asset-liability management, solvency standards, liquidity requirements, and insurance product contractual elements. Life insurers invest substantially in long-duration bonds and government debt because the guarantees incorporated in traditional policies and the structure of long-term liabilities make these assets crucial to portfolio creation. [10, 26, 30]. Insurance capital allocation should therefore be seen as climate-relevant portfolio positioning inside a strictly regulated balance-sheet architecture, rather than unconstrained voluntary green investing [31].

This balance-sheet reasoning is important for climate finance because it establishes the practical areas in which insurers might allocate resources. The literature on strategic asset allocation shows that climate considerations need to be integrated into long-term portfolio construction and scenario analysis, rather than being added later as a tactical environmental, social, governance (ESG) screen [32]. In this regard, Mercer [32] argues that standard strategic asset allocation models are poorly equipped to address climate change, since they rely heavily on historical relationships, while climate risk demands forward-looking scenario-based analysis. Similarly, the Forum for Responsible Investment [33] survey of Paris-market investors reports that ESG and climate criteria are increasingly treated as strategic-allocation issues and that the risk-management dimension remains fundamental, particularly for insurers operating under Solvency II constraints, a risk-based regulatory framework that requires insurers to maintain capital buffers in line with the risk profile of their assets. In this sense, climate-aligned capital allocation depends not only on investor intention, but on whether climate metrics, scenarios, and transition pathways are embedded into core portfolio design [32, 33].

Even when insurers attempt to boost climate-relevant investment, the literature identifies persistent barriers. Institutional investors' direct allocation to clean energy, resilient infrastructure, and other transition-supporting assets remains limited outside the largest and most sophisticated actors, owing to shortages of suitable vehicles, policy instability, unfamiliar risk profiles, and limited internal expertise [34]. This is consistent with Ameli et al. [11], who show that disclosure and transparency by themselves do not redirect capital toward public climate objectives. Climate-aligned capital allocation therefore depends on credible transition policy, investable pipelines, de-risking mechanisms, and institutional capacity—not simply on the presence of large pools of insurance capital [11, 34].

Green bonds are often presented as one of the most accessible channels through which insurers can support climate finance, especially because bonds fit insurers' liability structures and liquidity preferences. However, the literature suggests a more qualified interpretation. Jakubik and Uguz [19] find that green bond commitments by European insurers did not consistently generate strong positive market effects, while recent sectoral evidence shows that sustainability-labelled bonds still raise concerns around standards, verification, and the credibility of green labels [35]. At the same time, the same report shows that insurers' existing portfolios may remain materially exposed to fossil-fuel-related assets, with holdings concentrated among a relatively small number of firms. This underlines a central tension of capital allocation in insurance: insurers can support transition finance through green and resilience-oriented investment, but they may simultaneously continue financing carbon-intensive sectors unless portfolio realignment becomes broader and more systematic [19, 35].

The capital-allocation function is also important because it links climate finance to financial stability. Portfolio choices by insurers affect sovereign and corporate funding conditions, and under climate stress these choices can transmit shocks rather than merely absorb them. Corradin et al. [30] show that euro area insurers' holdings of sovereign bonds, home bias, and reliance on liquid government securities for claims funding can create spillovers into bond markets after natural disasters. More broadly, climate-related risks can interact with procyclical asset repricing, liquidity pressure, and reductions in insurance provision, with implications for the wider financial system (36]. For this reason, the asset-side contribution of insurers should be understood not only in developmental terms—as a source of long-term capital for mitigation, adaptation, and resilient infrastructure—but also in prudential and systemic terms. Insurers are not merely passive allocators of surplus funds; they are market-shaping institutions whose capital allocation decisions influence both the financing of climate solutions and the resilience of the financial system itself [30, 36].

Cross-Cutting Function

While this article is structured around three core dimensions, these do not operate independently. They are linked through a cross-cutting informational layer that includes risk pricing, catastrophe modelling, climate-risk assessment, scenario analysis, and the broader generation of climate-relevant information. One of the most significant contributions of insurers is precisely their role in translating physical climate risk into financial signals. Through premiums, underwriting conditions, exclusions, claims data, and forward-looking risk analytics, insurers make climate uncertainty economically legible [6].

This informational function is essential since financial flows are influenced by how risk is perceived, assessed, and priced in addition to the availability of capital. Capital may continue to flow toward susceptible assets, maladaptive investments may persist, and chances to increase resilience may be lost in situations where climate risk is poorly understood or not adequately reflected in financial decision-making [6, 9]. Insurers therefore contribute to climate finance not only through direct protection or investment, but also through the production of actionable information. In this way, they transform uncertain future climate impacts into signals that can influence behaviour, contractual arrangements, and investment decisions

For this reason, risk pricing, modelling, and the production of climate information should not be treated as a separate fourth pillar in competition with risk transfer, resilience, and capital allocation. Their analytical significance lies precisely in the fact that they underpin all three. They shape the terms under which risks are transferred, the incentives that support resilience, and the informational basis upon which capital is allocated. Conceptualising them as a cross-cutting function preserves the internal coherence of the tripartite framework while also recognising the foundational role of insurance information infrastructure in climate finance [6, 9].

Structural Constraints in Insurance Systems

The insurance sector plays an important role in climate finance, but its capacity is limited by a range of structural constraints, such as affordability challenges, uncertainty in future risk assessment, limited forward-looking modelling, and gaps in hazard and geographic coverage. Taken together, these constraints caution against overly optimistic expectations about what insurance can deliver under climate change, especially when reliance is placed primarily on pricing and market-based mechanisms. [37]. The first constraint is affordability. As climate risks intensify, premiums may rise beyond the reach of low-income households, farmers, small firms, or local governments. In such cases, the expansion of insurance does not necessarily reduce vulnerability; it may instead widen protection gaps between those who can afford coverage and those who cannot [5].

The second constraint concerns insurability. Certain risks may become so frequent, severe, or spatially correlated that they can no longer be sustainably covered through conventional insurance logic. This issue is particularly relevant for recurring disaster losses and slow-moving processes such as sea-level rise or desertification; as such risks do not fully align with traditional insurable risk models [18, 20]. As climate change alters the characteristics of hazard itself, the limitations of what can be privately insured may vary in ways that limit the sector's ability to provide comprehensive protection [38]. A third constraint is institutional unevenness. The climate-finance contribution of insurance is strongly reliant on regulatory capability, climate data availability, supervisory expectations, legal frameworks, and government support systems. Where these are inadequate or absent, the sector's contribution may stay limited, regardless of its theoretical capacity [39].

A fourth constraint concerns distribution. Insurance-based climate finance may work relatively well for well-capitalised actors, formalised markets, and asset-rich sectors, while leaving the most vulnerable populations outside effective systems of protection. This raises important questions about equity, access, and the social distribution of climate resilience [5, 13].

These constraints suggest that insurance should be understood as a complementary pillar of climate finance rather than as a substitute for public finance, concessional support, adaptation planning, or social protection. Its role is real and potentially substantial, but it depends on institutional design. Public-private partnerships, layered risk-sharing arrangements, premium support, public reinsurance, catastrophe pools, and stronger integration with adaptation strategies are all likely to shape whether insurance functions as an enabling component of climate finance or becomes a mechanism of exclusion and burden-shifting [5, 13].

4. Discussion

The literature reviewed in this article demonstrates that the insurance sector's role in climate finance is best understood through the interaction of risk transfer, resilience, and capital allocation. Although these functions are frequently discussed separately, bringing them together clarifies why insurance occupies a distinct position within climate finance architecture. The sector is neither reducible to a technical claims-paying industry nor adequately captured by its identity as a long-term institutional investor alone. Its distinctiveness lies in the fact that it operates simultaneously across multiple financial functions: absorbing and redistributing losses, shaping adaptation and recovery incentives, and allocating long-term capital in ways that affect transition and resilience pathways [5, 10].

The analytical value of the tripartite framework lies precisely in its ability to overcome fragmentation in the existing literature. Risk transfer emphasizes pre-arranged protection and post-shock liquidity to capture the financing of loss and recovery. However, the rich literature reviewed here also shows that this function is internally differentiated: capital-market-based transfer through catastrophe bonds or other insurance-linked structures is not comparable to the macro-financial significance of sovereign pools and public-private facilities, nor is the developmental significance of inclusive microinsurance [14, 17]. Bringing these layers together makes it clear why climate-finance research needs to consider not just the presence of cover but also instrument design, basis risk, public support, and the institutional architecture that converts claims-paying capability into resilience and recovery.

A central implication of this review is that climate finance should be interpreted more broadly than conventional measures of mitigation and adaptation spending often allow. Insurance demonstrates that climate finance is not limited to funds directed toward labelled projects. It also includes the financial arrangements through which societies absorb shocks, distribute losses,

structure recovery, and generate incentives for adaptation. In this sense, pre-arranged protection and post-disaster liquidity are part of climate finance, not external to it [3]. Likewise, the production of climate-risk information—through pricing, modelling, underwriting, and scenario analysis—is a constitutive dimension of how financial systems respond to climate uncertainty [6, 9]. At the same time, the research strongly cautions against exaggerating the importance of insurance. The sector does not provide a universal answer to climate financing gaps. Its effectiveness is dependent upon affordability, insurability, data, regulation, governance, and institutional coordination. Perhaps most crucially, the places and populations who require insurance-based resilience are frequently those where market provision is inadequate. This means that the future climate-finance role of insurance depends heavily on institutional design rather than market presence alone [5, 8]. Insurance can function as a strategic pillar of climate finance only when embedded within broader systems of public policy, adaptation planning, and layered risk-sharing.

Overall, the review points to a balanced conclusion. The insurance sector should neither be viewed as peripheral to climate finance, nor should it be regarded as capable of solving climate finance gaps on its own. It is best understood as a strategically important but bounded actor whose contribution depends on whether risk transfer, resilience-building, and capital allocation are institutionally aligned rather than treated as isolated functions [5, 13].

5. Conclusion

This review article has examined the role of the insurance sector in climate finance through three interconnected dimensions: risk transfer, resilience, and capital allocation. The analysis shows that the relevance of insurance to climate finance is already well established across multiple strands of scholarship, but remains unevenly conceptualised. Existing studies demonstrate that insurance can reduce the macroeconomic burden of climate catastrophes, support adaptation and preparedness, foster innovation in risk-transfer mechanisms, and participate in climate-relevant capital markets as a major institutional investor [8, 9, 20]. What has been less common, however, is to consider these contributions together within a single climate finance framework. By bringing them into one analytical structure, this article has argued that the insurance sector should be understood as a multifunctional climate finance actor rather than merely as a compensatory market institution.

The tripartite framework developed here also supports a more precise substantive conclusion regarding the three dimensions highlighted in the title. Risk transfer remains the most direct and visible contribution because it supplies pre-arranged liquidity, loss-sharing, and fiscal shock absorption after climate disasters. Yet the literature makes clear that its contribution depends heavily on instrument choice, risk layering, and institutional embedding: indemnity insurance, parametric products, sovereign pools, reinsurance, and capital-market instruments do not perform identical functions, and their effectiveness varies according to hazard type, data quality, affordability, and links with contingency planning and adaptation policy [16-18].

Resilience, in turn, should be understood as the dimension linking ex ante adaptation and preparedness to the broader financial architecture of climate risk management. The research demonstrates that insurance can promote resilience not just by providing post-disaster compensation but also by creating incentives for risk mitigation, promoting investments in adaptation, improving readiness, and developing climate-responsive goods and public-private partnerships [27]. However, because they rely on factors including affordability, price structures, regulatory design, data accessibility, and the degree to which insurance is integrated into broader adaptation plans, these effects are neither automatic nor uniformly distributed. Therefore, insurance contributes to resilience as an institutionally controlled process that aligns financial protection, behavioral incentives, and adaptation governance rather than as a stand-alone market outcome [37]. Capital allocation, meanwhile, should be understood as an asset liability management constrained but strategically consequential function. Insurers can help channel long-term finance toward renewable energy, green bonds, adaptation infrastructure, and broader transition pathways, yet this depends on portfolio design, solvency treatment, liquidity management, project availability, and the credibility of climate policy. The literature therefore supports a more precise conclusion: insurers matter as climate financiers not simply because they possess large balance sheets, but because they occupy a position where prudential portfolio choices can either accelerate climate-consistent capital reallocation or reproduce carbon-intensive lock-in [30, 32, 34, 35].

At the same time, the literature strongly cautions against overstating this role. Insurance cannot be expected to close climate finance gaps by itself. Affordability constraints, insurability problems, uneven regulatory capacities, weak investment incentives, and distributional exclusions all limit what the sector can achieve through market mechanisms alone [5, 13]. The future climate-finance role of insurance is therefore fundamentally a question of institutional design, not merely market scale. Public-private partnerships, premium support for vulnerable groups, public reinsurance mechanisms, catastrophe pools, climate-risk data infrastructure, and prudential frameworks that integrate climate scenarios all matter for whether insurance becomes an enabling mechanism of climate resilience or a source of exclusion.

For future research, the literature points toward several important directions. Further comparative research on how various legislative frameworks influence insurers' engagement in climate finance is required. The relationship between underwriting and investment choices inside insurance companies should also receive more attention, as these two aspects of the balance sheet are frequently discussed independently even though they are both crucial [40]. Lastly, a thorough examination of the distributive effects of insurance-led climate finance is necessary, especially in situations where market access is uneven and climate vulnerability is high [6, 11].

In general, the published literature supports a more robust and nuanced conclusion than what is often reflected in policy debates. The insurance sector is important not only because it provides compensation for losses related to climate finance,

but also because it shapes the ways in which climate risks are transferred, resilience is financed, and capital is directed in an environment of increasing uncertainty. Consequently, the sector's role is structurally significant, operationally diverse, and best understood in the context of political conditions. Therefore, insurance should be treated not as a subsidiary element but as a central one in today's climate finance discussions.

Competing Interest / Conflict of Interest

The author declares no conflict of interest.

Acknowledgements

The author has no acknowledgements to declare.

6. References

[1] Climate Policy Initiative. (2021). Building climate resilience in cities through insurance. https://www.climatepolicyinitiative.org/publication/building-climate-resilience-in-cities-through-insurance/ (Accessed: 20/08/2025)

[2] Zhang, D., Mohsin, M., Rasheed, A. K., Chang, Y., & Taghizadeh-Hesary, F. (2023). Climate finance: What we know and what we should know? Economic Analysis and Policy, 77, 759–782.

[3] IPCC. (2022). Climate change 2022: Mitigation of climate change. Contribution of Working Group III to the Sixth Assessment Report of the Intergovernmental Panel on Climate Change. Cambridge University Press.

[4] Seçkin Codal, K., & Codal, A. (2022). Sosyal medyada iklim değişikliği tartışmaları. Efe Akademi Yayınevi.

[5] OECD. (2023). Enhancing the insurance sector's contribution to climate adaptation. Enhancing the insurance sector's contribution to climate adaptation, OECD Business and Finance Policy Papers, OECD Publishing, Paris.

[6] Geneva Association. (2021). Climate change risk assessment for the insurance industry. https://www.genevaassociation.org/sites/default/files/climate_risk_web_final_250221.pdf (Accessed: 24/08/2025)

[7] Nobanee, H., Dilshad, M. N., Abu Lamdi, O., Ballool, B., Al Dhaheri, S., AlMheiri, N., Alyammahi, A., & Alhemeiri, S. S. (2022). Insurance for climate change and environmental risk: A bibliometric review. International Journal of Climate Change Strategies and Management, 14(5), 440–461.

[8] Nobanee, H., & Nghiem, X.-H. (2024). Climate catastrophe insurance for climate change: What do we know and what lies ahead? Current Opinion in Environmental Sustainability, 66, 101395. https://doi.org/10.1016/j.cosust.2023.101395

[9] Gupta, A., & Venkataraman, S. (2024). Insurance and climate change. Current Opinion in Environmental Sustainability, 67, 101412.

[10] Golnaraghi, M. (2018). Climate change and the insurance industry: Taking action as risk managers and investors. The Geneva Association.https://www.genevaassociation.org/sites/default/files/research-topics-document-type/pdf_public/ climate_change_and_the_insurance_industry_-_taking_action_as_risk_managers_and_investors.pdf (Accessed: 10/09/2025)

[11] Ameli, N., Drummond, P., Bisaro, A., Grubb, M., & Chenet, H. (2020). Climate finance and disclosure for institutional investors: Why transparency is not enough. Climatic Change, 160, 565–589.

[12] Rothwell, M., Earle, M., Ooi, C. H., Orr, J., Shroff, S., & Siew, J. (2020). Practical guide to climate change for general insurance practitioners. British Actuarial Journal, 25, e18.

[13] OECD. (2025). Scaling finance and investment for climate adaptation. OECD Publishing. https://www.oecd.org/content/dam/oecd/en/publications/reports/2025/07/scaling-finance-and-investment-for-climate-adaptation_be6892fb/eeec8b52-en.pdf (Accessed: 16/11/2025)

[14] Surminski, S. (2013). The role of insurance risk transfer in encouraging climate investment in developing countries. In P.-M. Dupuy & J. E. Vinales (Eds.), Harnessing foreign investment to promote environmental protection (pp. 228–250). Cambridge University Press.

[15] United Nations Environment Programme Finance Initiative & Principles for Sustainable Insurance Initiative. (2021). Guidance on the Task Force on Climate-related Financial Disclosures (TCFD) for the insurance sector. https://www.unepfi.org/psi/wp-content/uploads/2021/01/PSI-TCFD-final-report.pdf (Accessed: 11/10/2025)

[16] Le Quesne, F., Tollmann, J., Range, M., Balogun, K., Zissener, M., Bohl, D., Souvignet, M., Schuster, S., Zwick, S., Phillips, J., Wehnert, B., & Kreft, S. (2017). The role of insurance in integrated disaster and climate risk management: Evidence and lessons learned. Munich Climate Insurance Initiative. https://www.shareweb.ch/site/DRR/Documents/Types%20of%20activity/Risk%20Transfer/Report_Insurance_Integrated_Disaster_Climate_Risk_Management_2017_GIZ_English.pdf (Accessed: 19/09/2025)

[17] UNDP. (2025). Climate and disaster risk finance and insurance (CDRFI) in national adaptation plans and nationally determined contributions: Analytical report. United Nations Development Programme. https://climatepromise.undp.org/

sites/default/files/research_report_document/CDRFI%20in%20NAPs%20and%20NDCs_26%20June.pdf (Accessed: 16/11/2025)

[18] Balogun, K. (2014). Applicability of risk transfer tools to manage loss and damage from slow-onset climatic risks. Procedia Economics and Finance, 18, 710–717.

[19] Jakubik, P., & Uguz, S. (2021). Impact of green bond policies on insurers: Evidence from the European equity market. Journal of Economics and Finance, 45(2), 381–393.

[20] Giuzio, M., Rousová, L., Kapadia, S., Kumar, H., Mazzotta, L., Parker, M., & Zafeiris, D. (2025). Climate change, catastrophes, insurance and the macroeconomy. European Economic Review, 173, 105210.

[21] Cleary, P., Harding, W., McDaniels, J., Svoronos, J.-P., & Yong, J. (2019). Turning up the heat: Climate risk assessment in the insurance sector. Financial Stability Institute Insights on Policy Implementation, No. 20. https://www.bis.org/fsi/publ/insights20.pdf (Accessed: 28/08/2025)

[22] Schanz, K.-U. (2023). The re/insurance perspective on disaster resilience. Environment Systems and Decisions, 43, 535–536.

[23] Jarzabkowski, P., Chalkias, K., Clarke, D., Iyahen, E., Stadtmueller, D., & Zwick, A. (2019). Insurance for climate adaptation: Opportunities and limitations. Global Commission on Adaptation. https://www.gca.org/reports/insurance-for-climate-adaptation-opportunities-and-limitations/ (Accessed: 21/10/2025)

[24] ClimateWise. (2021). Climate product innovation within the insurance sector. University of Cambridge Institute for Sustainability Leadership & Deloitte. https://www.cisl.cam.ac.uk/files/climatewise_climate_product_innovation.pdf (Accessed: 14/10/2025)

[25] Mikaelsson, M. (2026). Insurance and reinsurance under climate stress: Managing systemic risk in global supply chains. Stockholm Environment Institute.

[26] IAIS. (2025). Application paper on the supervision of climate-related risks in the insurance sector. International Association of Insurance Supervisors. https://www.iais.org/uploads/2025/04/Application-Paper-on-the-supervision-of-climate-related-risks-in-the-insurance-sector.pdf (Accessed: 24/09/2025)

[27] Roper, J. A., Casagrande, D. G., & Bocchini, P. (2025). Climate change and insurance: Embracing resilience for private market survival. Sustainable Development, 33, 8499–8510.

[28] Xu, Z., Fang, H., & Wang, W. (2025). The impact of climate risk on insurers' sustainable operational efficiency: Empirical evidence from China. Sustainability, 17(8), 3423.

[29] Yang, Q., Lemanski, M. K., & Watters, C. (2025). The impact of climate change on the insurance industry: Perceptions of industry experts and corporate responses. Journal of Risk and Financial Management, 18(9), 516.

[30] Corradin, S., Fontana, A., Kubitza, C., & Maddaloni, A. (2025). Insurance companies in the euro area: Asset allocation and impact on financial markets. ECB Discussion Paper Series, No. 28. https://www.ecb.europa.eu/pub/pdf/scpdps/ecb.dp28~03966255e7.en.pdf (Accessed: 20/11/2025)

[31] Kouwenberg, R. Strategic asset allocation for insurers under Solvency II. J Asset Manag 19, 447–459 (2018). https://doi.org/10.1057/s41260-018-0097-4

[32] Mercer. (2011). Climate change scenarios: Implications for strategic asset allocation. Mercer, IFC, and Carbon Trust. https://documents1.worldbank.org/curated/en/138101493381025955/pdf/114650-IFC-Brief-Mercer-web-PUBLIC.pdf (Accessed: 18/10/2025)

[33] Forum pour l'Investissement Responsable. (2020). Integrating ESG-climate issues into asset allocation: Challenges and practices. https://www.frenchsif.org/isr_esg/actus/2020/FIR-Asset-Allocation-Integrating-ESG–climate-ssues_October2020.pdf (Accessed: 13/11/2025)

[34] Kaminker, C., & Stewart, F. (2012). The role of institutional investors in financing clean energy. OECD Working Papers on Finance, Insurance and Private Pensions, No. 23.

[35] Ceres, Persefoni, & ERM. (2023). Changing climate for the insurance sector: Research and insights. https://www.sustainability.com/globalassets/sai-changing-climate-for-insurance_final.pdf (Accessed: 25/10/2025)

[36] FSB. (2020). The implications of climate change for financial stability. Financial Stability Board. https://www.fsb.org/uploads/P231120.pdf (Accessed: 19/10/2025)

[37] Ingels, M. W., Botzen, W. J. W., Aerts, J. C. J. H., Brusselaers, J., & Tesselaar, M. (2024). The state of the art and future of climate risk insurance modeling. Annals of the New York Academy of Sciences, 1541(1), 100–114. https://doi.org/10.1111/nyas.15255

[38] Charpentier, A. (2008). Insurability of climate risks. Geneva Papers on Risk and Insurance – Issues and Practice, 33(1), 91–109.

[39] He, Q., & Faure, M. (2022). Adaptation to climate change risks and regulation through insurance: The case of China. Climate Law, 12(2), 162–183.

[40] Chen, B., Liang, Z., & Pang, S. (2025). Dynamic investment-driven insurance pricing and optimal regulation. Insurance: Mathematics and Economics, 125.

Kastamonu University
Journal of Engineering and Sciences
e-ISSN 2667-8209
http://dergipark.gov.tr/kastamonujes

Numerical Investigation of the Aerodynamic Characteristics of a .40 S&W JHP Bullet

Rıza Cem Kılıç[a,*], Fatih Cellek[a], Emrah Kantaroğlu[a]

[a] Department of Mechanical Engineering, Faculty of Engineering and Natural Science, Kirikkale University, Kirikkale, Türkiye
***Corresponding Author:** rcemkilic@gmail.com

Received: **April 22, 2026** ◆ Accepted: **June 15, 2026** ◆ Published Online: **June 24, 2026**

Abstract: The external-ballistic behaviour of a projectile is governed by the drag forces acting on it throughout flight; accurate prediction of the drag coefficient (C_d) is therefore critical for trajectory and range calculations. However, the drag coefficient of the .40 S&W JHP bullet has not been reported in the literature and its open hollow-point nose is not represented by the standard drag-law families that assume conventional ogival profiles. This gap is compounded by the operating velocity of the round (352 m/s, Mach ≈ 1.02), which lies in the transonic regime, where shock formation and base separation make the drag coefficient particularly difficult to estimate. To address this gap, this study determines the drag coefficient of the .40 S&W JHP bullet through a three-dimensional Computational Fluid Dynamics (CFD) external-flow analysis based on NIJ 0101.06 reference conditions. The simulations were performed in ANSYS Fluent under the ideal-gas assumption, using the k-ω SST turbulence model with a wall-resolved near-wall mesh ($y^+ \approx 0.94$) and a grid-independence study. The numerical analysis yielded a drag coefficient of $C_d = 0.255$. The flow field exhibited a pronounced pressure difference between the high-pressure stagnation region at the nose cavity ($\approx 1.09\times10^5$ Pa) and the low-pressure wake behind the base ($\approx 4.39\times10^4$ Pa), while the local Mach number reached 1.39 at the nose, indicating shock-wave formation; these results show that pressure drag is the dominant component of the total aerodynamic resistance. The original contribution of this work is that it provides, for the first time, a geometry-specific C_d for this widely used round in the transonic regime and quantifies the influence of the hollow-point cavity on its drag behaviour. The reported value provides a reference for external-ballistic trajectory prediction and for the design of ballistic test setups relevant to body-armour evaluation.

Keywords: External ballistics, CFD, Drag coefficient, .40 S&W JHP bullet, Ballistic test setup, ANSYS Fluent

40 S&W JHP Mermisinin Aerodinamik Özelliklerinin Sayısal Incelenmesi

Öz: Bir merminin dış balistik davranışı, uçuş boyunca üzerine etki eden sürükleme kuvvetleri tarafından belirlenir; bu nedenle sürükleme katsayısının (C_d) doğru tahmini, yörünge ve menzil hesaplamaları açısından kritik öneme sahiptir. Ancak .40 S&W JHP merminin sürükleme katsayısı literatürde raporlanmamış olup, merminin açık oyuk uçlu burnu, geleneksel ojival profilleri varsayan standart sürükleme yasası ailelerince temsil edilmemektedir. Bu eksiklik, merminin çalışma hızının (352 m/s, Mach ≈ 1,02) transonik rejimde yer almasıyla daha da belirginleşmektedir; bu rejimde şok oluşumu ve taban ayrılması, sürükleme katsayısının tahminini özellikle güçleştirmektedir. Bu eksikliği gidermek amacıyla, bu çalışmada .40 S&W JHP merminin sürükleme katsayısı, NIJ 0101.06 referans koşulları temel alınarak üç boyutlu Hesaplamalı Akışkanlar Dinamiği (HAD) dış akış analizi yoluyla belirlenmektedir. Simülasyonlar, ideal gaz varsayımı altında ANSYS Fluent ortamında; duvar-çözümlü duvar yakını ağ ($y^+ \approx 0,94$) ile k-ω SST türbülans modeli ve bir ağdan bağımsızlık çalışması kullanılarak gerçekleştirilmiştir. Sayısal analiz, Cd = 0,255 değerinde bir sürükleme katsayısı vermiştir. Akış alanı, burun kovuğundaki yüksek basınçlı durma bölgesi ($\approx 1,09\times10^5$ Pa) ile taban arkasındaki düşük basınçlı iz bölgesi ($\approx 4,39\times10^4$ Pa) arasında belirgin bir basınç farkı sergilemiş; yerel Mach sayısı burunda 1,39'a ulaşarak şok dalgası oluşumuna işaret etmiştir. Bu sonuçlar, basınç sürüklemesinin toplam aerodinamik direncin baskın bileşeni olduğunu göstermektedir. Bu çalışmanın özgün katkısı, yaygın olarak kullanılan bu mermi için transonik rejimde ilk kez geometriye özgü bir C_d değeri sunması ve oyuk uçlu kovuğun sürükleme davranışı üzerindeki etkisini niceliksel olarak ortaya koymasıdır. Raporlanan değer, dış balistik yörünge tahmini ve vücut zırhı değerlendirmesine yönelik balistik test düzeneklerinin tasarımı için bir referans sağlamaktadır.

Anahtar Kelimeler: Dış akış, HAD, Sürükleme katsayısı, .40 S&W JHP mermi, Balistik test düzeneği, ANSYS Fluent

1. Introduction

External ballistics, which examines the path a bullet follows through the air from the moment it leaves the barrel until it strikes the target, is a fundamental discipline in assessing the accuracy and range of ammunition. A bullet's flight path is determined by its ballistic coefficient—which varies depending on the bullet's mass, caliber and shape—as well as fundamental launch parameters such as initial velocity and launch angle. From the moment the bullet leaves the barrel, it is subjected to the complex interaction of gravitational forces and the drag forces created by the fluid medium (air). In particular, environmental conditions such as air temperature and pressure directly alter the air resistance the bullet experiences, significantly affecting its flight time and trajectory. To accurately solve the "encounter problem" between the bullet and the target and ensure the target is hit accurately, a precise analysis of environmental factors and fluid interactions during free flight is an absolute necessity [1,2].

The aerodynamic behavior of projectiles plays a critical role in determining their motion in external ballistics. One of the most important parameters affecting projectile performance is the drag coefficient (C_d), which directly influences the resistance encountered during flight [3]. Accurate determination of the drag coefficient is essential for understanding projectile aerodynamics, especially in cases where experimental data is limited. In the literature, drag coefficient values for specific ammunition types such as the .40 S&W JHP bullet are scarce or unavailable. Therefore, numerical methods such as Computational Fluid Dynamics (CFD) have become widely used for predicting aerodynamic characteristics [4].

Beyond ballistics, Computational Fluid Dynamics (CFD) has become a well-established tool for resolving complex flows dominated by separation, recirculation and strong near-wall gradients, provided that an appropriate turbulence closure, a wall-resolved mesh and a systematic grid-independence and validation procedure are employed [5-8]. Recent thermohydraulic investigations illustrate this methodology clearly: numerical and experimental analyses of concavity-dimpled surfaces have shown how a concave cavity controls local stagnation, recirculation and turbulent kinetic energy [5]; wall-resolved ($y^+ \approx 1$) models combined with grid-independence testing and experimental validation have quantified the flow and transport in dimpled and corrugated tubes [6]; and the same simulate-then-validate framework has been applied to channelled flows with engineered geometries [7]. The present study adopts these same methodological standards turbulence model selection suited to the flow regime, near-wall resolution with $y^+ < 1$, mesh-independence verification and benchmarking against available data and transfers them to the external transonic flow around the .40 S&W JHP projectile, whose hollow-point cavity produces an analogous interplay of stagnation, recirculation and wake-driven drag.

In this study, a Computational Fluid Dynamics (CFD) analysis of the .40 S&W JHP projectile was conducted based on the NIJ0101.06 – Type II test configuration, at the standard velocity of 352 m/s (Mach ≈ 1.02) and standard atmospheric conditions, using the k-ω SST turbulence model with a fully wall-resolved near-wall mesh ($y^+ \approx 0.94$) and a grid-independence study to ensure solution reliability. The study is motivated by a specific gap in the literature: the drag coefficient of the .40 S&W JHP bullet has not been reported and its open concave nose is not represented by the standard drag-law families that assume conventional ogival profiles [9]. This gap is compounded by the operating regime of the round, since at 352 m/s the flow is transonic, where shock formation and base separation make the drag coefficient particularly difficult to estimate and most sensitive to the nose geometry. The novelty of the work is therefore twofold: it provides the first geometry-specific C_d for this widely used round in the transonic regime and it quantifies how the hollow-point cavity governs the pressure-drag and wake behaviour that standard drag models cannot capture. The resulting drag coefficient offers a validated reference for external-ballistics trajectory prediction and for the design and instrumentation of ballistic test setups relevant to body-armour evaluation.

2. Material and Method

Geometric Modelling

The geometry of the .40 S&W JHP bullet was modelled in ANSYS SpaceClaim based on the projectile dimensions considered in this study. The geometric modelling stages and dimensional details of the projectile are presented in Figure 1. The 3D model of the .40 S&W JHP bullet is shown in Figure 1(a), while the complete cartridge model is presented in Figure 1(b). In addition to the projectile model, an external flow enclosure was generated around the bullet to represent the surrounding air domain.

The geometric dimensions of the projectile model are consistent with the nominal specifications of the .40 S&W cartridge as defined in SAAMI Z299.3, with a bullet diameter of 10.17 mm (0.400 in) [10]. The main dimensional parameters used in the modelling process are shown in Figure 1(c). The radial cuts of the hollow point cavity were incorporated based on the reference CAD geometry [11], as no standardized dimensional specification exists for this manufacturer-specific feature. These hollow-point details can be observed in Figure 1(a) and Figure 1(c). Although the minor geometric features of the hollow point cavity were retained in the model, their aerodynamic contribution at transonic speeds is considered negligible compared with the dominant effects of the frontal cavity, ogive surface and base separation region.

The .40 S&W cartridge is manufactured with several distinct nose geometries, including Full Metal Jacket Round Nose (FMJ-RN), Flat Nose (FMJ-FN), Truncated Cone (FMJ-TC), Total Metal Jacket (TMJ), Soft Point (JSP), Semi-Wadcutter (SWC) and Jacketed Hollow Point (JHP), each producing fundamentally different external flow characteristics [12–14]. Among these,

the JHP geometry was selected for this analysis because it uniquely combines three aerodynamically distinct surface features within a single body: an open concave nose cavity that generates a well-defined stagnation region and measurable pressure asymmetry at the leading face, a continuously curved ogive suitable for boundary-layer development studies, and a sharp-edged flat base that produces a clean, well-defined wake and separation zone for base-drag modelling [13,14]. These characteristic geometric features are clearly visible in Figure 1(a) and Figure 1(c). In contrast, simpler profiles such as the FMJ-RN provide a smooth, featureless nose that limits the complexity and academic value of the resulting flow field [12], while FMJ-FN and SWC geometries, despite incorporating a flat meplat, lack the internal recirculating cavity flow that makes the JHP configuration particularly advantageous for CFD validation and drag decomposition across the transonic regime in which the .40 S&W operates [12–14].

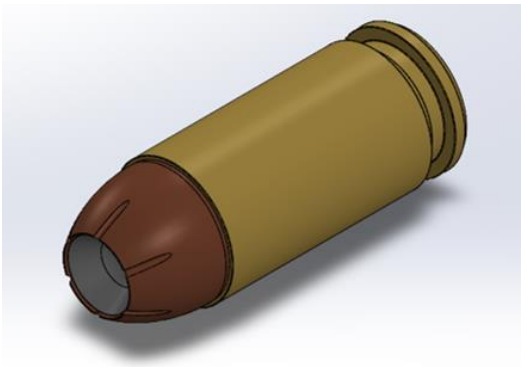

(a)

(b)

(c)

Figure 1. Geometric modelling and dimensional representation of the .40 S&W JHP bullet cartridge: (a) 3D model of the .40 S&W JHP bullet [11], (b) 3D model of the .40 S&W JHP bullet cartridge, and (c) dimensional measurements of the .40 S&W JHP bullet cartridge. The nominal bullet diameter was checked according to SAAMI Z299.3 [10]

An external flow enclosure was generated around the projectile to define the computational domain. The dimensions of the enclosure were selected as multiples of the projectile length (L) in order to minimize boundary effects and ensure proper flow development. The upstream distance was defined as 2L, the downstream distance as 10L and the radial distances as 5L in the transverse directions [12]. The calculation domain is shown in Figure 2.

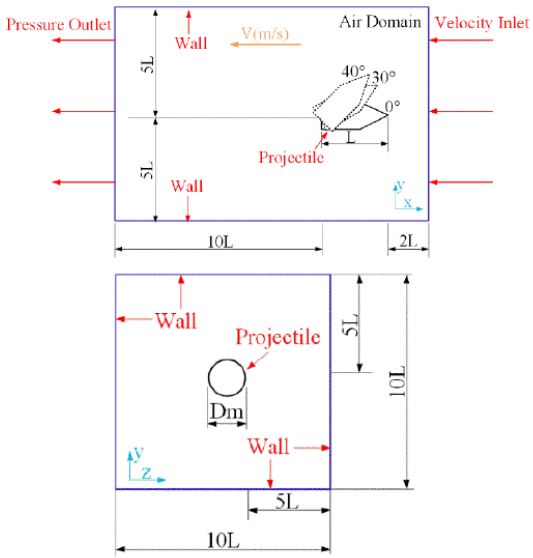

Figure 2. Calculation domain base dimensions [12]

In addition, a Body of Influence (BOI) was defined around the projectile to locally refine the mesh in regions with high velocity and pressure gradients. As illustrated in Figure 3, the BOI volume surrounds the projectile and covers the near-field flow domain, where boundary-layer development, flow separation and wake formation are expected to be dominant. This local refinement strategy improves the resolution of the critical flow regions without significantly increasing the overall computational cost.

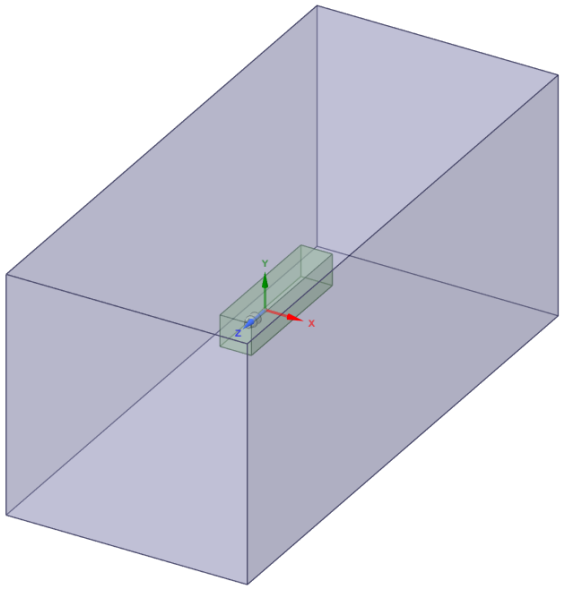

Figure 3. Geometry with the Body of Influence (BOI) volume around the projectile

Mesh

In this study, the numerical mesh for the .40 S&W JHP bullet geometry was generated using ANSYS Fluent. A hybrid mesh approach was adopted to effectively represent both the near-wall regions of the complex bullet geometry and the far-field flow domain. An overview of the computational domain and the generated mesh structure is presented in Figure 4.

To locally refine the mesh resolution in regions of high flow gradients, particularly around the bullet nose, body, boat-tail and wake region, the Body of Influence (BOI) method was applied. The BOI approach defines a dedicated control volume surrounding the bullet geometry, within which the mesh element size is maintained significantly smaller than that of the outer flow domain. This allows sufficient resolution to be achieved in critical flow regions without unnecessarily increasing the total element count.

The near-wall mesh was carefully configured to ensure accurate resolution of the boundary-layer flow behaviour. As shown in Figure 5, inflation layers were generated on the projectile surface to resolve the near-wall flow field. Consistent with the requirements of the selected k-ω SST turbulence model [15], a dimensionless wall distance of $y+ \approx 0.94$ was achieved. This value satisfies the $y+ < 1$ criterion, within which the k-ω SST model is capable of directly resolving the viscous sublayer, thereby enabling high-fidelity boundary-layer analysis without the need for wall functions.

To verify that the numerical solution is independent of the mesh structure, a mesh-independence study was conducted using four different mesh density levels. For each mesh level, the drag coefficient (Cd) was computed at a bullet velocity of 352 m/s (Mach ≈ 1.02), determined in accordance with the NIJ 0101.06 Type II standard [16], and the results were comparatively evaluated. The computed Cd values, together with the corresponding mesh parameters, are presented in Figure 6. The mesh level at which the variation in Cd values with increasing mesh density fell below a defined threshold was identified as the optimal mesh configuration, providing a balance between computational efficiency and solution accuracy. This mesh configuration was subsequently employed in all simulations.

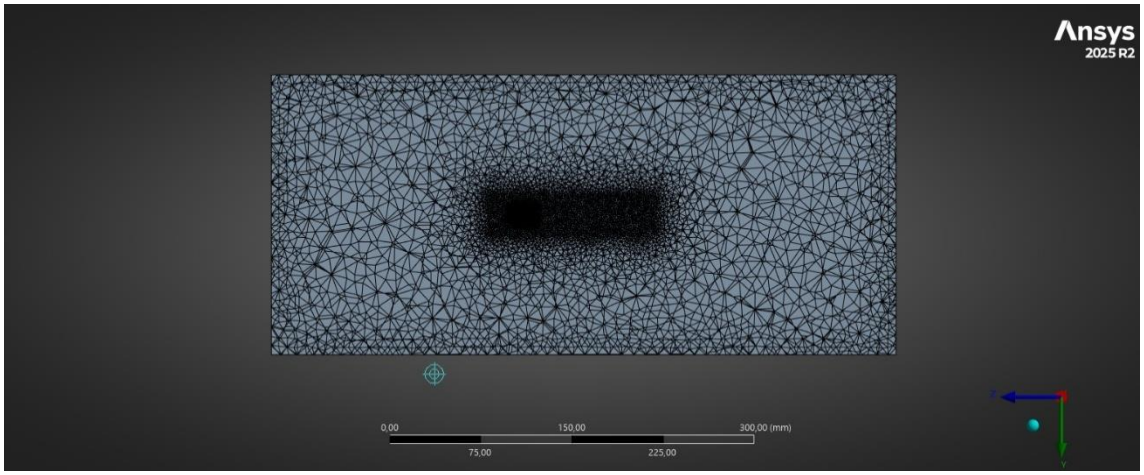

Figure 4. Overview of the computational domain and mesh structure

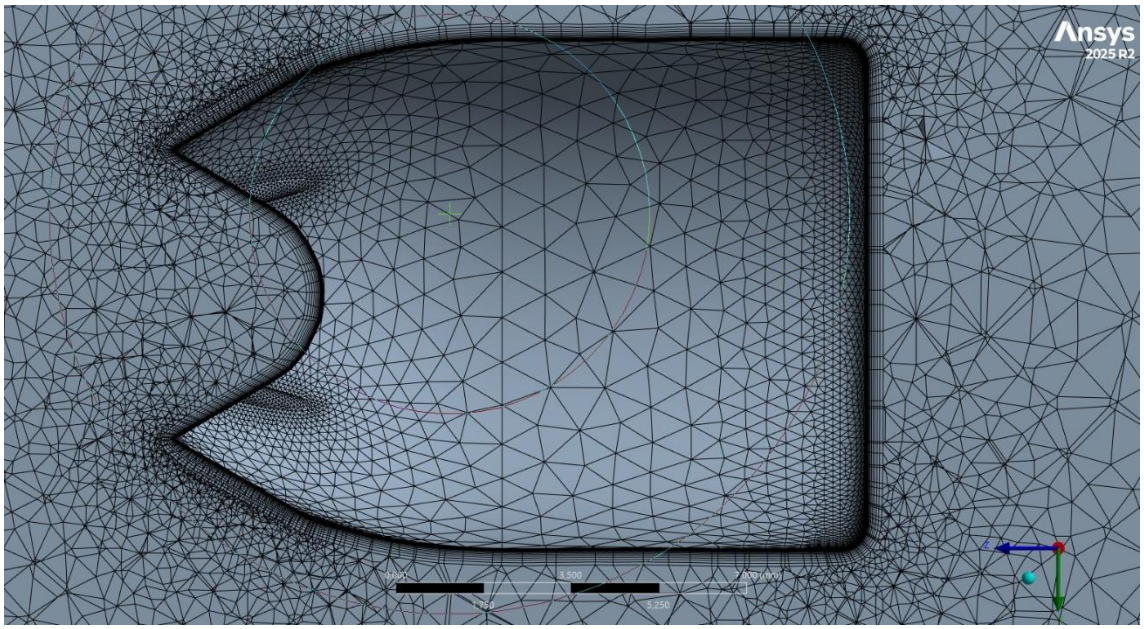

Figure 5. Detailed view of the surface mesh and inflation layers on the projectile body

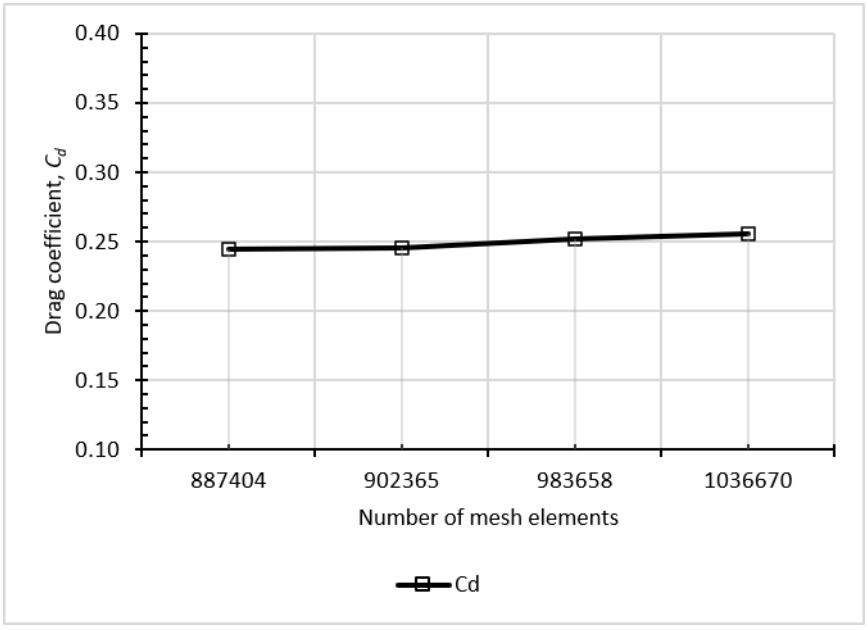

Figure 6. Drag coefficient for different mesh

Numerical Setup

All simulations were carried out using ANSYS Fluent. Air was defined as the working fluid under the ideal gas assumption, which allows density variations to be captured as a function of local pressure and temperature. A necessary consideration for flows in the transonic regime [17].

Turbulence closure was achieved using the k-ω SST model, which has been widely adopted in projectile aerodynamics studies due to its reliable performance in predicting flow separation and adverse pressure gradient effects at transonic speeds [15, 18].

Ambient conditions were set in accordance with the NIJ0101.06 – TYPE II standard, with a temperature of 21°C and a reference pressure of 101,325 Pa [16]. A velocity inlet boundary condition of 352 m/s (Mach ≈ 1.02) was applied at the domain inlet, while a pressure outlet condition was imposed at the downstream boundary. All projectile surfaces were treated as no-slip walls and the analysis was conducted as a full 3D simulation. The numerical setup parameters are summarized in Table 1 and the boundary conditions applied to the computational domain are illustrated in Figure 7.

Table 1. Numerical setup parameters

Parameter	Value
Working Fluid	Air (Ideal Gas)
Turbulence Model	k-ω SST
Ambient Temperature	21 [°C]
Reference Pressure	101,325 Pa
Inlet Velocity	352 m/s (Mach ≈ 1.02)
Outlet Condition	Pressure Outlet
Wall Condition	No-slip Wall

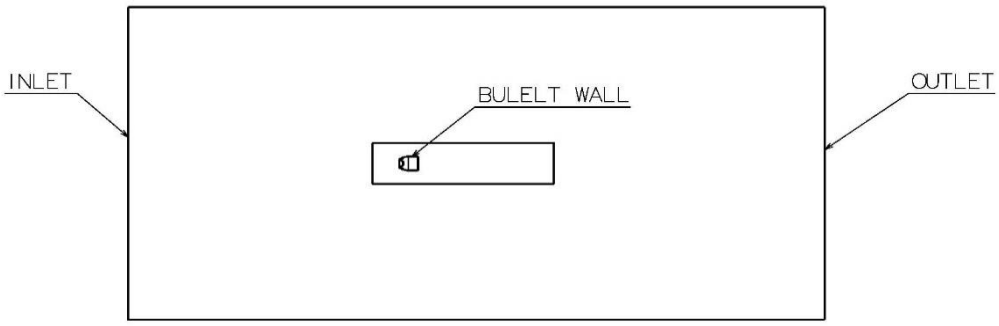

Figure 7. Computational domain and boundary conditions

3. Results

The external flow field around the .40 S&W JHP projectile at Mach ≈ 1.02 was numerically investigated and aerodynamic characteristics were determined using ANSYS Fluent.

Pressure Distribution

As illustrated in Figure 8, the static pressure distribution around the .40 S&W JHP projectile exhibits a distinct high-pressure stagnation region at the hollow-point cavity of the projectile nose, reaching a maximum value of 1.09×10^5 Pa. The pressure then drops sharply along the ogive surface and decreases to 4.39×10^4 Pa in the low-pressure wake region behind the projectile base. This pronounced pressure difference between the nose and base constitutes the primary source of pressure drag, which represents the dominant component of the total aerodynamic resistance acting on the projectile [18,19].

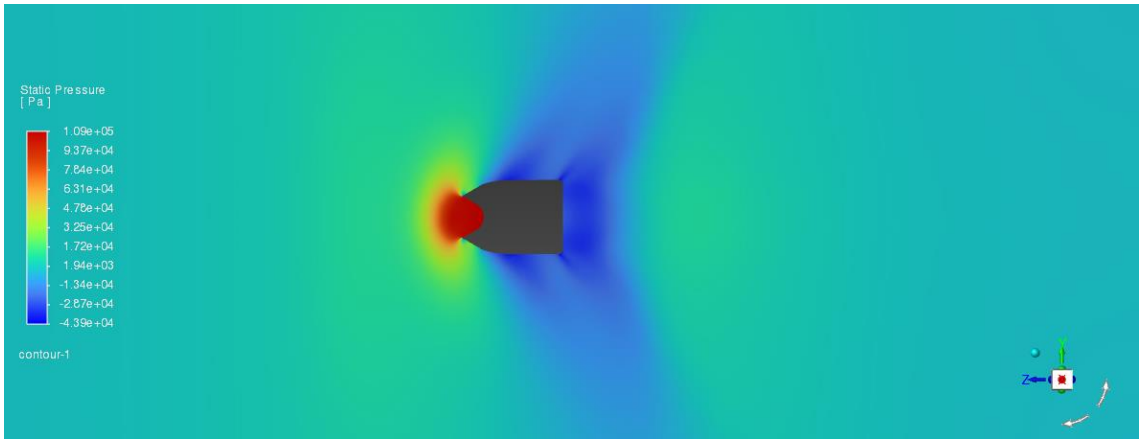

Figure 8. Static pressure distribution around the .40 S&W JHP projectile

Velocity Distribution

As shown in Figure 9, the velocity magnitude contour indicates that the flow velocity decreases to nearly zero within the bullet nose cavity, forming a stagnation point. Along the ogive surface, the flow accelerates, and the local velocity reaches up to 444 m/s around the projectile [18]. The velocity vector distribution presented in Figure 10 further confirms the formation of a low-velocity recirculation wake region immediately behind the bullet base.

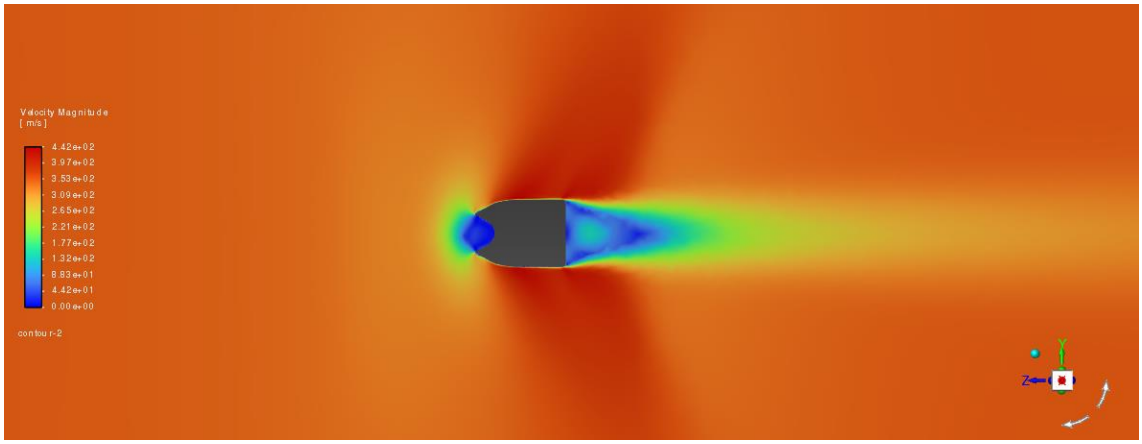

Figure 9. Velocity magnitude contour around the projectile

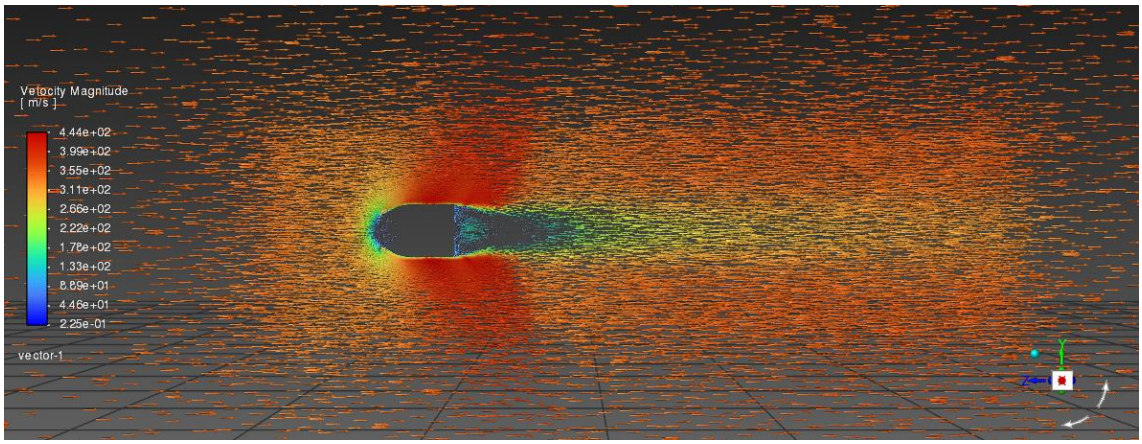

Figure 10. Velocity vectors around the projectile

Pathlines

As shown in Figure 11, the pathlines coloured by velocity magnitude indicate that the free stream exhibits an orderly flow structure along the bullet axis. The flow entering the nose cavity undergoes partial compression within the cavity, leading to the formation of a recirculating flow structure. Downstream of the bullet base, a distinct wake region develops, and the flow characteristics in this region confirm the presence of base drag [9,18].

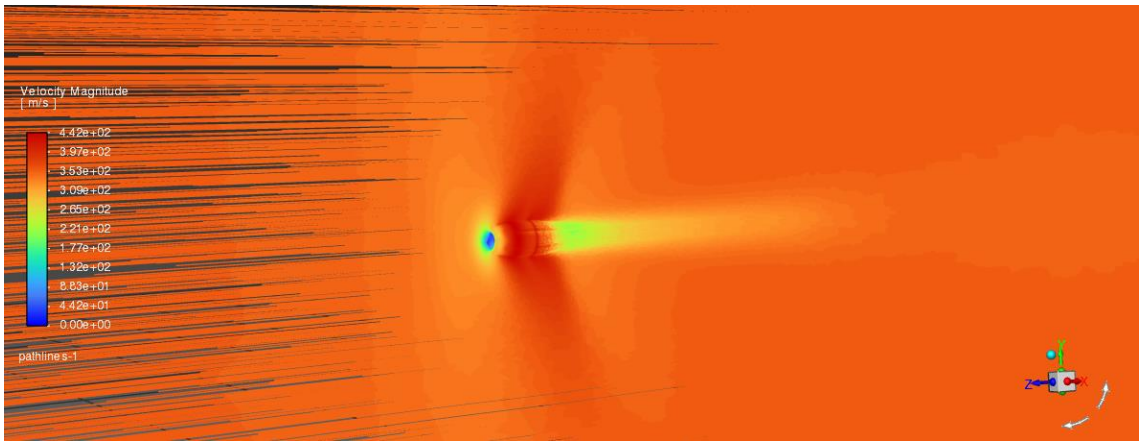

Figure 11. Pathlines colored by velocity magnitude

Mach Number Distribution

The Mach number distribution presented in Figure 12 demonstrates the influence of the transonic flow regime around the bullet. In the nose region, the local Mach number reaches up to 1.39, indicating the formation of a shock-wave structure. Behind the bullet base, the Mach number decreases significantly, which reflects the low-energy nature of the wake region. The shock-wave formation observed in the transonic flow field increases the contribution of wave drag to the overall aerodynamic resistance [17,18].

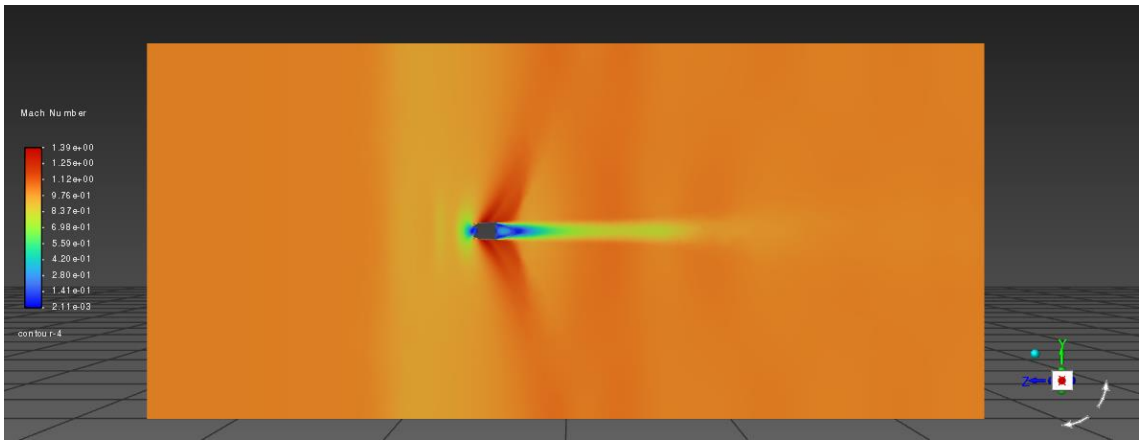

Figure 12. Mach number distribution around the projectile

Turbulent Kinetic Energy

The turbulent kinetic energy distribution presented in Figure 13 shows that the highest turbulence intensity is concentrated in the wake region behind the bullet base. The maximum turbulent kinetic energy in this region is 1.01×10^4 m²/s². In contrast, the turbulence level remains negligible in the free-stream region, indicating that the k-ω SST model successfully captures the transition between the undisturbed flow and the wake region [15].

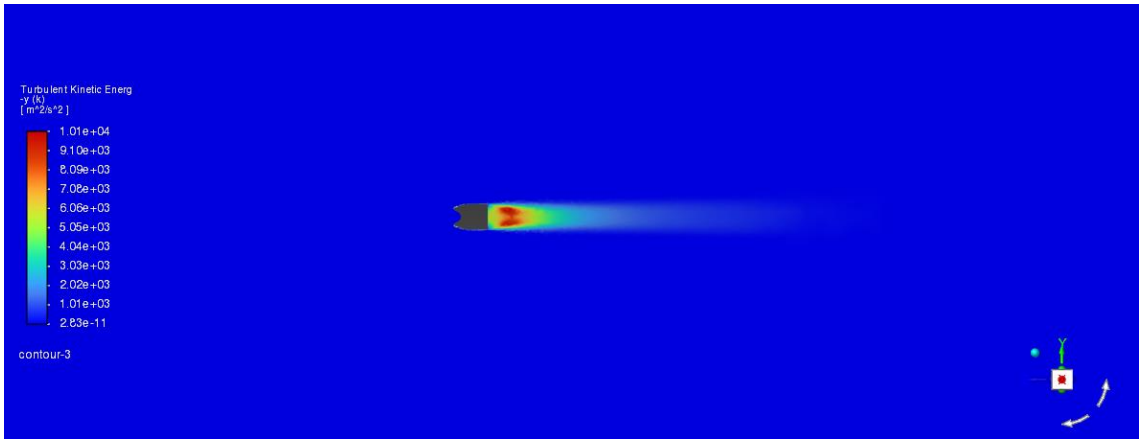

Figure 13. Turbulent kinetic energy distribution

Drag Coefficient

As a result of the numerical analysis, the drag coefficient of the .40 S&W JHP bullet at Mach ≈ 1.02 was determined as C_d = 0.255. The value is consistent with the range of drag coefficients reported in the literature for bullets of similar caliber and geometry in transonic regimes. Since no directly comparable reference value for the .40 S&W bullet is available in the literature, this study is considered provides an original contribution [9, 18].

4. Discussion

In this study, the aerodynamic behavior of the .40 S&W JHP projectile was analyzed using CFD under NIJ0101.06 – Type II conditions (352 m/s, Mach ≈ 1.02), determining a drag coefficient (C_d) of 0.255.

Results show that pressure drag is the dominant component of the total aerodynamic resistance. The JHP's concave nose creates a high-pressure stagnation point (1.09×10^5 Pa), while a low-pressure wake region behind the base (4.39×10^4 Pa) causes significant base drag. Additionally, a local Mach number of 1.39 at the nose indicates shock wave formation, which contributes to wave drag in the transonic regime. The k-ω SST turbulence model successfully captured these complex boundary layer and wake dynamics using a high-resolution hybrid mesh ($y^+ \approx 0.94$).

Given the lack of existing data for this specific ammunition, the calculated C_d of 0.255 provides a reliable and consistent reference for external ballistics. Future research should focus on the experimental validation of these numerical results and expanding the analysis to other aerodynamically distinct nose geometries, such as FMJ and SWC.

Table 2. Drag coefficient comparison

Bullet	Mach	Cd
.40 S&W JHP	Mach 1.02	0.255
.223 Rem FMJ [4]	Mach 0.9	0.137
.223 Rem FMJ [4]	Mach 1.1	0.426
G1 [4]	Mach 1.00	0.245
G7 [4]	Mach 1.05	0.422

To place the computed drag coefficient in context, the present value was compared with reported transonic drag data for representative projectiles and standard drag-law models, as summarised in Table 2. The present Cd of 0.255 at Mach ≈ 1.02 lies within the range of reported transonic values and is close to the G1 standard drag function at Mach 1.00 (Cd ≈ 0.245), consistent with a position on the lower flank of the transonic drag rise. The steep increase between Mach 0.9 and 1.1 for the .223 Rem case (0.137 to 0.426) and the higher value of the G7 model (0.422 at Mach 1.05) reflect the well-known sensitivity of the drag coefficient to Mach number in this regime, where a small change in Mach can more than double Cd. A direct one-to-one comparison is nevertheless limited: the reference cases differ in nose and base geometry and the G1/G7 values represent standard drag functions normalised to their own reference geometries rather than object-specific frontal-area coefficients. The present result should therefore be interpreted as being consistent with the expected transonic range rather than as a one-to-one match and experimental validation of the computed coefficient is identified as a priority for future work.

5. Conclusion

In this study, the drag coefficient of the .40 S&W JHP projectile was determined through a 3D CFD external-flow analysis under NIJ 0101.06 reference conditions using the k-ω SST model with a wall-resolved mesh ($y^+ \approx 0.94$) and a grid-independence study. The drag coefficient at Mach ≈ 1.02 was found to be $C_d = 0.255$, the first geometry-specific value reported for this round. Pressure drag was the dominant component of the total aerodynamic resistance, arising from the difference between the high-pressure stagnation region at the hollow-point cavity and the low-pressure wake behind the flat base. A local Mach number of 1.39 at the nose confirmed shock-wave formation and the contribution of wave drag in the transonic regime, while the maximum turbulent kinetic energy was concentrated in the near-base wake, consistent with the base-drag mechanism. The computed value lies within the range of transonic drag coefficients reported for comparable projectiles and standard drag functions and is close to the G1 value at Mach 1.0, indicating a position on the lower flank of the transonic drag rise.

The significance of these results is twofold. Methodologically, they demonstrate that pressure drag, rather than skin friction, governs the aerodynamic behaviour of short, flat-based hollow-point projectiles in the transonic regime, so that the nose-cavity and base geometry are the primary levers determining their drag. Practically, the reported C_d provides a reference value that can be used directly as an input for external-ballistic trajectory prediction and for the design and instrumentation of ballistic test setups relevant to NIJ type body armour evaluation, where geometry-specific data for this round were previously unavailable.

Future work should prioritise the experimental validation of the computed drag coefficient, for example through Doppler-radar or aeroballistic-range measurements. Beyond this, the analysis could be extended from a single operating point to a full C_d–Mach curve spanning the subsonic-to-supersonic range and the same framework could be applied to the other nose geometries of the .40 S&W family (FMJ-RN, FMJ-FN, SWC) to enable a comparative assessment of their drag characteristics.

Competing Interest / Conflict of Interest

The authors declare that they have no competing interests.

Author Contribution

We declare that all Authors equally contribute.

Acknowledgements

The author has no acknowledgements to declare.

6. References

[1] Egorov, S. F. (2024). Electronic shooting simulator family" STrIzh": research of mathematical models on target point determiners of entry and basic levels. Devices and Methods of Measurements. 5(4): 295-306.

[2] Egorov S. F., & Shelkovnikov Y. K. (2022). Shooting simulator «inhibitor»: ballistic software «meeting tasks». Intellekt. Sist. Proizv. 20(2): 114–127.

[3] Yunus, A. C. (2010). Fluid Mechanics: Fundamentals And Applications (Si Units). Tata McGraw Hill Education Private Limited.

[4] Maxa, J., Šabacká, P., Bayer, R., Binar, T., Bača, P., Švecová, J., Talár, J., Vlkovský, M., & Dobšáková, L. (2025). The tuning of a CFD model for external ballistics, followed by analyses of the principal influences on the drag coefficient of the. 223 rem caliber. Technologies. 13(5), 190.

[5] Al-Haidari, S. R., Al-Obaidi, A. R., Saleh, Z. M., Mohammed, A., & Ismail, H. B. (2025). Enhancement of thermohydraulic performance in 3D pipe based on different concavity dimpled surfaces: Numerical and experimental investigation. Case Studies in Thermal Engineering. 75, 107153.

[6] Al-Haidari, S. R., & Al-Obaidi, A. R. (2025). Extensive investigation of hydrothermal flow and heat performance improvement in a 3D tube based on varying concavity dimple and corrugation turbulator configurations. Heat Transfer. 54(5): 3134-3162.

[7] Saleh, Z. M., & Al-Haidari, S. R. (2026). Numerical investigation of the effect of central inlet–dual outlet arrangement and sidewall fin shapes on the thermal-hydraulic performance of multi-channels cold plate. International Communications in Heat and Mass Transfer. 173, 110835.

[8] Alhaidari, S. R., Razzaq, A. M., & Al-Obaidi, A. R. (2025). Numerical analysis of the flow field and improvement heat transfer based on varying dimple parameter configurations in 3D tube. In AIP Conference Proceedings. 3350(1), 070006.

[9] McCoy, R. (1999). Modern exterior ballistics: The launch and flight dynamics of symmetric projectiles. Schiffer Military History. https://www.mori.bz.it/Balistica/Mc%20Coy%20Modern%20Exterior%20Ballistic.pdf

[10] Sporting Arms and Ammunition Manufacturers' Institute. (2022). ANSI/SAAMI Z299.3 – Centerfire pistol & revolver. https://saami.org/technical-information/ansi-saami-standards/

[11] Bartosz Rakowski. (2022). .40 S&W [CAD model]. GrabCAD. https://grabcad.com/library/40-s-w-2

[12] Hao, B., Jiang, Q., Xu, C., & Liu, L. (2024). Aerodynamic characterization of bullet heads with different arcuate curves. Journal of Applied Fluid Mechanics. 17(5): 1015-1026.

[13] Gan, C. (2021). Computational fluid dynamics (CFD) of drag force for bullet's shape design. In Journal of Physics: Conference Series. 1888(1), 012016.

[14] Khan, A., Shah, I., Aziz, S., Waqas, M., Zaman, U. K. U., & Jung, D. W. (2022). Numerical and experimental analysis of drag and lift forces on a bullet head. Aerospace. 9(12), 816.

[15] Menter, F. R. (1994). Two-equation eddy-viscosity turbulence models for engineering applications. AIAA journal. 32(8): 1598-1605.

[16] National Institute of Justice. (2008). Ballistic resistance of body armor (NIJ Standard-0101.06 Type II). U.S. Department of Justice. https://www.ojp.gov/pdffiles1/nij/223054.pdf

[17] John D. Anderson. (2003). Modern compressible flow: With historical perspective (3rd ed.). McGraw-Hill.

[18] Silton, S. I. (2002). Navier-Stokes computations for a spinning projectile from subsonic to supersonic speeds. Army Research Laboratory.

[19] Hoerner, S. F. (1965). Fluid Dynamic Drag, published by the author. Midland Park, NJ, 16-35.